SANDIA REPORT

SAND2005-6522
Unlimited Release
Printed October 2005

Experimental and Computational Study of the Liquid–Solid Transition in Tin

Jean-Paul Davis and Stephen Foiles

Prepared by
Sandia National Laboratories
Albuquerque, New Mexico 87185 and Livermore, California 94550

Sandia is a multiprogram laboratory operated by Sandia Corporation,
a Lockheed Martin Company, for the United States Department of Energy's
National Nuclear Security Administration under Contract DE-AC04-94AL85000.

Issued by Sandia National Laboratories, operated for the United States Department of Energy by Sandia Corporation.

Available to DOE and DOE contractors from
U.S. Department of Energy
Office of Scientific and Technical Information
P.O. Box 62
Oak Ridge, TN 37831

Telephone: (865)576-8401
Facsimile: (865)576-5728
E-Mail: reports@adonis.osti.gov
Online ordering: http://www.osti.gov/bridge

Available to the public from
U.S. Department of Commerce
National Technical Information Service
5285 Port Royal Rd
Springfield, VA 22161

Telephone: (800)553-6847
Facsimile: (703)605-6900
E-Mail: orders@ntis.fedworld.gov
Online order: http://www.ntis.gov/help/ordermethods.asp?loc=7-4-0#online

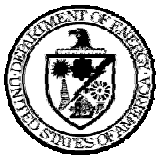

SAND2005-6522
Unlimited Release
Printed October 2005

Experimental and Computational Study of the Liquid–Solid Transition in Tin

Jean-Paul Davis
Shock and Z-Pinch Physics

Stephen Foiles
Computational Materials Science and Engineering

Sandia National Laboratories
P.O. Box 5800
Albuquerque, NM 87185-1181

Abstract

An experimental technique was developed to perform isentropic compression of heated liquid tin samples at the Z Accelerator, and multiple such experiments were performed to investigate solidification under rapid compression. Preliminary analyses, using two different methods, of data from experiments with high uncertainty in sample thickness suggest that solidification can begin to occur during isentropic compression on time scales of less than 100 ns. Repeatability of this result has not been confirmed due to technical issues on the subsequent experiments performed. First-principles molecular-dynamics calculations based on density-functional theory showed good agreement with experimentally-determined structure factors for liquid tin, and were used to investigate the equation of state and develop a novel interatomic pseudo-potential for liquid tin and its high-pressure solid phase. Empirical-potential molecular-dynamics calculations, using the new potential, gave results for the solid-liquid interface velocity, which was found to vary linearly with difference in free energy between the solid and liquid phases, as well as the liquidus, the maximum over-pressurization, and the solid-liquid interfacial energy. These data will prove useful in future modeling of solidification kinetics for liquid tin.

ACKNOWLEDGEMENTS

Jean-Paul Davis would like to acknowledge Paul Vianco (Org. 1824) and Ron Goeke (Org. 2452) for extensive advice concerning thin-film coatings and their reactions with surrounding materials, as well as Jerry Knorovsky (Org. 1813), Charlie Robino (Org. 1813), and John Stephens (Org. 1825) for important information concerning molybdenum metallurgy. A number of technicians and engineers have been involved in the development of the resistive pre-heating system: Randy Hickman (Org. 1646) and Josh Mason (Org. 1646) of Sandia; Doug DeVore, Chuck Dickerson, Paul Flores, Matt Gurule, Chris Jeffs, Morris Kaufman, Mike Madlener, Mitchell Parks, Jerry Taylor, Aric Tibbitts, Phil Watts, and Charlie Wright of Bechtel Nevada; Kevin Youngman and Alberto Pirela of Ktech; Allen Elsholz, Jim Emig, and Tim Uphaus of Lawrence Livermore National Laboratory. In addition, thanks go to the huge team of people in Z Operations and Z Supporting Technologies that make experiments on Z possible. Independent contractor Dennis Hayes developed the three-phase continuum model for tin.

Stephen Foiles would like to acknowledge many useful discussions with J. J. Hoyt (Org. 1814) concerning the simulation of solid-liquid interfaces. Aidan Thompson (Org. 1435) incorporated the new interatomic potential into the parallel molecular dynamics code, GRASP. Finally, Marcus Martin (Org. 1435) provided important advice on the use of the DAKOTA software package for the determination of interatomic potentials.

This work was in large part performed under the Laboratory Directed Research & Development (LDRD) Program (Project 52739), and in its entirety supported by the United States Department of Energy's National Nuclear Security Administration, operated by Sandia Corporation, a Lockheed Martin Company, under contract DE-AC04-94AL85000.

CONTENTS

1. INTRODUCTION

The behavior of materials under dynamic high-pressure conditions is directly relevant to stockpile stewardship. In particular, there is a programmatic need for, as well as high scientific interest in, improved understanding of dynamic solidification behavior under high pressures. The shock physics organization in Center 1600 of Sandia National Laboratories began in 2001 to undertake experiments to isentropically compress molten tin (Sn) under dynamic conditions using the Z and Saturn Accelerators. Tin was chosen primarily for its relatively low melting temperature. Diagnostics for this type of experiment consist solely of interferometric velocity measurements at sample/window interfaces, which can be difficult to relate to actual physical processes occurring in the sample. For materials undergoing structural phase transitions, typical analyses of experimental results consist of simulating the experiment with a model for the phase transition and determining whether that model is consistent with the measured velocity histories.

The isentropic compression experiment (ICE) technique [Hall *et al*, 2001] developed at Sandia has the potential to achieve thermodynamic states not possible under more traditional impact techniques for dynamic loading, as shown in Figure 1-1 for Sn. Impact experiments would produce shocked states on the Hugoniot, which for 600-K initial temperature in Sn are in the mixed-phase region at lower peak pressures, but come back into the liquid state at higher pressures due to entropic heating effects of the shock wave. For an equilibrium (instantaneous) transformation from liquid to solid, however, a ramped ICE compression wave can bring the tin to a thermodynamic state well inside the region of stability for the γ-solid phase. (The γ phase has a simple body-centered tetragonal, or BCT structure.) For a very slow transition far from equilibrium, the tin might follow the metastable path shown in Figure 1-1. Real dynamic solidification will depend on the kinetics of various mechanical processes such as nucleation and growth of the solid phase in the liquid matrix.

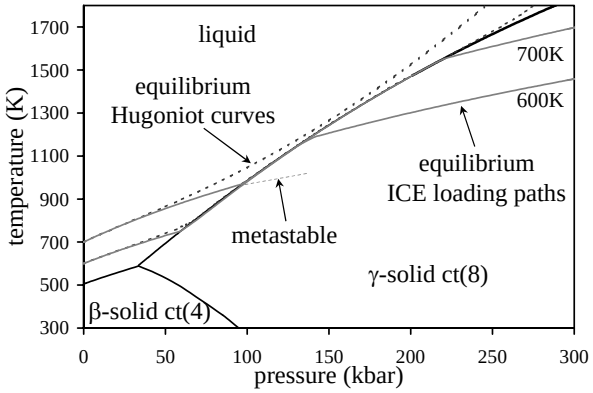

Figure 1-1: Equilibrium phase diagram of Sn computed from thermodynamics using EOS parameters from Mabire and Héreil (2000) showing equilibrium Hugoniot curves (dashed) and ICE loading paths (solid gray) for initial temperatures of 600K and 700K.

To help gain a deeper understanding of the dynamic solidification process, a joint Laboratory Directed Research and Development (LDRD) project was begun in Fall of 2002 between Centers 1600 and 1800. The goal of this project was to investigate rapid solidification in tin on a microscopic scale using a molecular-dynamic (MD) computational technique, and, where possible, apply computational results to the design and analysis of isentropic compression experiments. Results from *ab initio* MD were to provide data for fitting a pseudo-potential to use in MD calculations with larger systems appropriate for studying solidification. The original project proposal included investigation of a liquid–liquid structural transition in tin; early experiments suggested this possibility, and such transitions have been seen in phosphorous [Katayama *et al*, 2000] and carbon [Glosli and Ree, 1999].

This report describes both experimental and computational advances made during the three years of LDRD Project 52739. Section 2 describes the experimental approach and the many technical issues encountered that have thus far prevented acquisition of a complete set of trustworthy, repeatable experimental data on liquid tin. Section 3 presents all experimental measurements to date on isentropic compression of liquid tin, and conclusions drawn from analyses of some of these data. Section 4 discusses the computational approach, and Section 5 the computational results. A brief summary with suggestions for future work is given in Section 6.

2. EXPERIMENTAL APPROACH

An isentropic compression loading experiment (ICE) technique has been developed at Sandia Labs using the Z pulsed-power accelerator to provide ramped, planar, magnetic pressure loading of material samples over durations of several hundred nanoseconds [Hall *et al*, 2001]. In brief, the Z accelerator produces a pulse of electrical current, typically 10-20 MA in magnitude and having 100-300 ns rise time; when discharged through a low-inductance coaxial load shorted at one end, this pulse generates a strong time-varying magnetic force on the outer electrode (anode on Z), as shown in Figure 2-1. Planarity and uniformity of magnetic pressure across 6-12 mm (laterally) are obtained by using a square or rectangular load configuration with a narrow gap between the electrodes. For high-conductivity anode materials, the ramped stress wave outruns diffusion of the magnetic field so that at any given time of interest, a region of material (colored green in Figure 2-1) has been processed only by the stress wave and not by any electromagnetic effects such as joule heating.

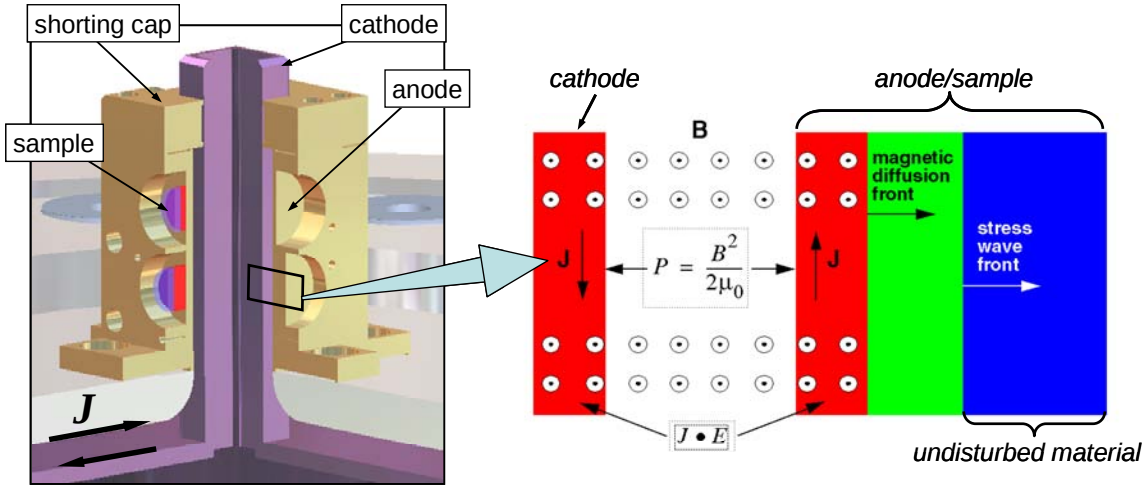

Figure 2-1: Rectangular coaxial load used on the Z machine to produce planar, ramped compression waves (*B* is magnetic field, *J* is current density, *P* is magnetic pressure).

The ramped loading technique is ideally suited to the study of structural phase transitions under dynamic compression, especially those not accessible by Hugoniot measurements (including solidification transitions as discussed in Section 1). The shape of a propagated ramp wave is sensitive to the derivative of the material's stress-strain response, and hence to the details of any phase transition and its kinetics. A ramp wave also steepens as it propagates through materials having normal compressibility (*i.e.*, stiffness increases with compression), and this is exacerbated by large variations in wave speed typical of materials undergoing phase transitions. In the case of solidification, shock formation limits the propagation distance for which a transition signature appears. For typical dimensions of Z experiments, solidification can only be detected if its overall rate is greater than 10^7 s^{-1}.

Typical diagnostics consist of time-resolved velocity measurements at material/vacuum or material/window interfaces on samples bonded to the outside of the anode plates, or on the anode material itself. Velocity is measured using a Velocity Interferometer System for Any Reflecting Surface (VISAR) in push-pull mode [Hemsing, 1979]. Due to space constraints, experiments on Z typically use bare-fiber probes to illuminate and collect reflected light from the samples, which limits probe efficiency to the order of 1%. A transparent window is required to directly measure the velocity of liquid tin; two well-characterized materials typically used are c-axis sapphire (single-crystal Al_2O_3) and lithium fluoride (LiF). Neither material matches the acoustic impedance of tin, which falls intermediate between the two. Simultaneous measurements of wave propagation under two different boundary conditions, however, may help shed light on the solidification process.

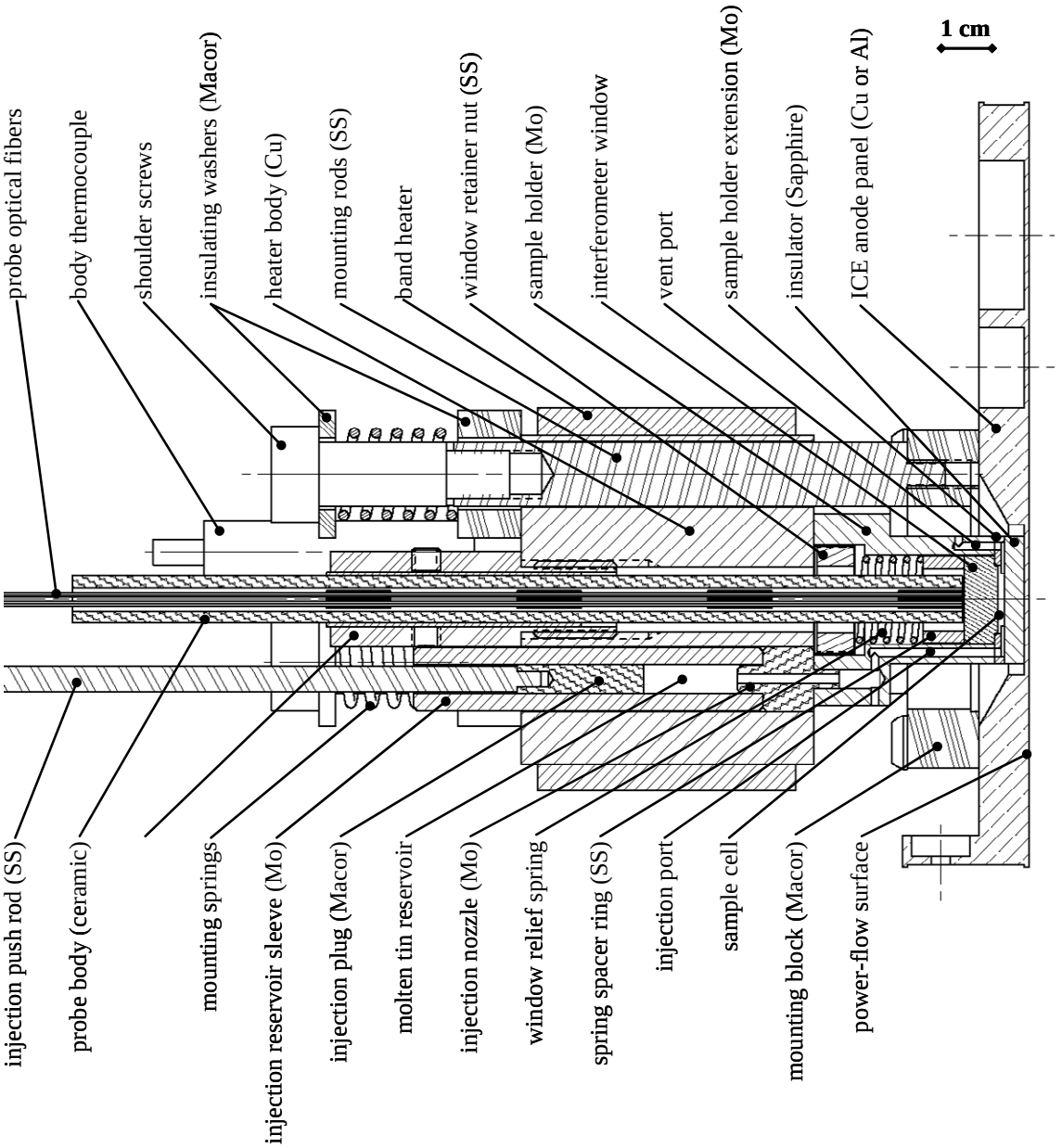

Figure 2-2: Scale cross-section drawing of the resistive pre-heat apparatus (single-sample version) mounted to a typical ICE drive panel, with all parts labeled (SS = stainless steel).

The basic design of the apparatus to pre-heat molten tin samples for Z experiments is described in Section 2.1, while a more detailed accounting of individual technical issues that arose during development and fielding of the apparatus is given in Section 2.2.

2.1. Resistive Pre-Heating Apparatus for Z

Beyond simply heating the tin sample to a known, controlled temperature, the apparatus for pre-heated experiments on Z must meet a number of requirements, some peculiar to the ICE technique. These requirements include the following: knowing the liquid sample thickness to an accuracy of a

few microns (ICE samples are typically less than 0.5 mm thick); ensuring the liquid sample is free of voids, as high purity as possible, and of uniform temperature; and maintaining an adequate reflector at the sample/window interface for VISAR measurements. The VISAR probes must withstand elevated temperatures. One significant difference from impact-type experiments is that the heated sample is in good thermal and mechanical contact with a massive heat sink in the form of the Z machine's power-flow structure. Because even micron-size voids in the path of a propagating ramp wave will change the shape of that wave, any additional material interfaces between the anode electrode and the sample must remain void-free when heated. Finally, thermal distortions of the anode could affect symmetry and uniformity of the magnetic pressure.

A detailed cross-sectional drawing of one version of the apparatus used at Z is presented in Figure 2-2. The particular geometry shown was used on experiments executed in the summer of 2003, but the labels indicate the materials used in more recent designs. A 250-Watt Tempco® band-type resistance heater provides the heating energy. The copper heater body transfers heat to the sample holder, houses a reservoir of molten tin, and provides a base on which to mount optical-fiber VISAR probes. The molybdenum sample holder assembly is clamped against a sapphire insulator disc (which itself is bonded to the anode panel) using springs to relieve thermal expansion. The sapphire minimally perturbs a propagating compression wave. The mounting block is made of Macor,® a machinable ceramic, for thermal insulation and mechanical stability. A top-hat-shaped interferometer window is clamped inside the sample holder against a 1.0-mm thick sample holder extension that has been brazed to the main part of the sample holder. The window is made of either sapphire or LiF; spring loading of the window prevents damage from thermal stresses, particularly for LiF which has a large coefficient of thermal expansion and cleaves very easily. The sample cell dimensions are defined in the lateral direction by the inner diameter of the sample-holder extension (6.9 mm diameter), and in the axial direction by the insulator and window surfaces (0.3-0.7 mm depending on window top-hat height). Nickel films on both the window and insulator promote wetting while forming a solid intermetallic bond layer through which further diffusion is slowed [de Avillez *et al*, 1996], preventing complete dissolution of the film into the bulk tin during the experiment wait time (which can in rare cases exceed one hour).

The injection hardware is used in a small vacuum chamber, off-line from the Z Accelerator, to prepare tin samples in advance of an experiment using different panel and insulator hardware. The samples are injected against a glass ceramic insulator having just enough surface roughness to promote mechanical wetting, and are initially prepared thicker than desired using a temporary extension to the sample holder. The small, contorted vent port at the top of the sample holder provides a vacuum path while minimizing evaporation of the molten tin. After cooling to room temperature very slowly under vacuum, the samples in their sample holders are precision machined to the final thickness. Actual thickness for a particular molten sample on an experiment is determined by metrology of the sample holder and sprung window assembly prior to casting the sample and again after final machining, and by accounting for thermal expansions of the sample holder and window.

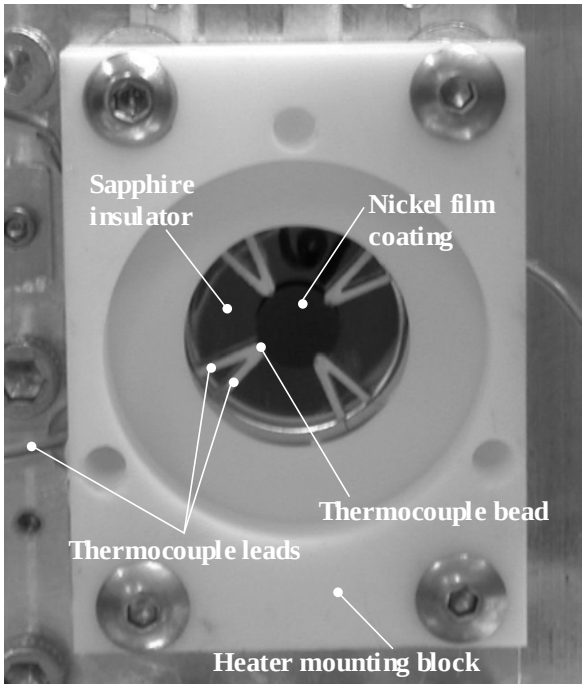

Figure 2-3: Heater mounting block and thermocouple-instrumented sapphire insulator installed on an anode panel.

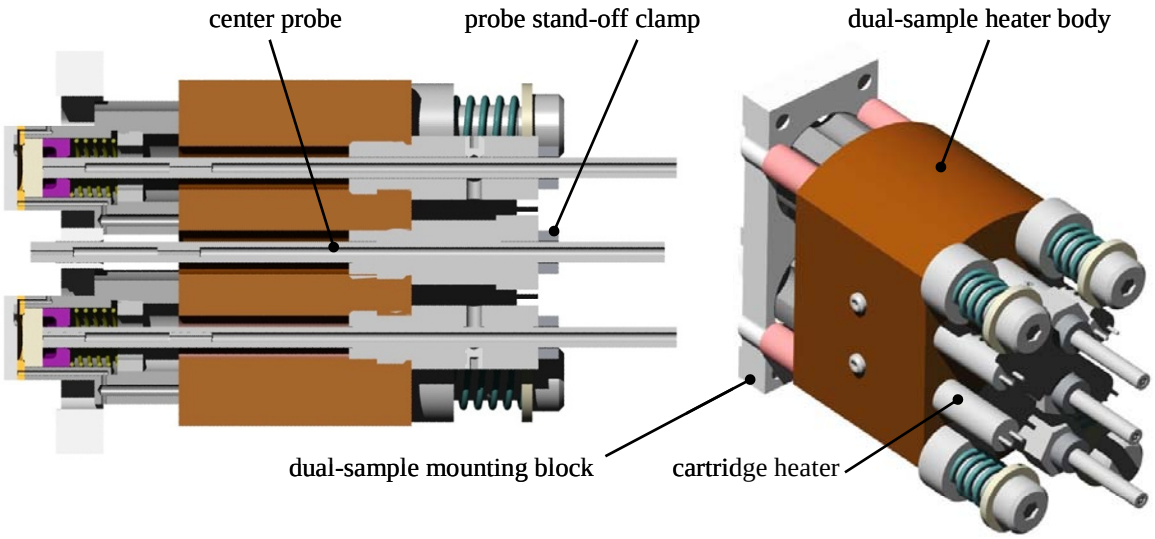

Figure 2-4: Dual-sample pre-heat geometry used on later Z experiments (anode panel is not shown).

The temperature of the molten tin is measured by two to four redundant fine-gauge (75-μm diameter leads) type-K thermocouples, bonded into V-shaped pairs of grooves machined in the surface of the sapphire insulator, as shown in Figure 2-3. High-temperature Aremco® cement thermally and electrically insulates each lead in its own groove, with the thermocouple beads at the point of each V left exposed to the molten tin. The bead junctions are distributed on a 5.3-mm diameter circle.

Many of the most recent experiments used the dual-sample geometry depicted in Figure 2-4. This design eliminates the band heater in favor of four ¼" cartridge heaters (also from Tempco®), and allows heating of up to eight samples per shot using only four heater bodies. The addition of a probe stand-off clamp allows one to precisely set the stand-off distance between the window and the front of the probe using a feeler gauge. The heater body accepts a third central VISAR probe to measure motion of the anode plate in the center of the panel, which aids in analysis of data from the samples. Sample preparation is performed individually in each sample holder using a set-up similar to that in Figure 2-2. The final section of the injection channel consists of a slot in the temporary injection extension, so that the sample has no connection to the reservoir after final machining.

The power duty cycle of the heater is controlled remotely using an Omega® CNi-series PID (Proportional-Integral-Derivative) controller with feedback provided by a thermocouple either in the heater body or in contact with the sample. Hardware, software, and infrastructure have been implemented at the Z Accelerator to allow for independent control of up to four heater cells per shot, with up to four individual cartridge or band heaters per cell. Up to 40 thermocouples can be recorded, including those used for feedback control. Approximately 5-10 seconds prior to the shot on Z, all connections between the load and the screen box housing the control unit are isolated using remotely controlled relays in order to avoid damage to components in the screen box from the electromagnetic pulse generated by Z. The change in temperature during this time is generally less than 1-2 K.

Sample-to-sample temperature differences are limited to approximately 200 K by poor conduction into the accelerator's stainless-steel power-flow structure and resultant heating of the anode panels through the sapphire insulators. Several design variations are available to passively control heat flow in the anode panels. To reduce heat flow between panels, ceramic insulators are placed along their lateral edges. To make the panels heat up to a higher, more uniform temperature, ceramic insulators are placed along their top and bottom edges. Finally, to increase heat flow out of the panels, a copper heat sink apparatus is attached to the shorting cap. This last design feature can be used in conjunction with lateral panel insulators.

2.2. Technical Design Issues

Development of the pre-heating system for isentropic compression experiments on liquid tin followed a slow trial-and-error process, in part because any truly comprehensive test requires a shot on Z, and opportunities to use the system at Z were infrequent. The purpose of this section is to document the design issues encountered, how they have been addressed, and their current status.

2.2.1. Temperature Control

Problems related to controlling the sample temperature arose on a number of the pre-heat experiments at Z, giving sample temperatures significantly higher or lower than desired. Various causes for these problems have been identified to include the following: heating delay when control thermocouples are not co-located with heaters; PID control parameters not tuned properly for the shot configuration; insufficient electrical supply to power all heaters simultaneously; damaged components in the control unit; crossed wires in the cabling; heating of samples on cooler panels by hotter panels; and improperly seated dual-sample heaters due to sapphire insulators having mismatched thickness.

In the present system, feedback control always relies on two redundant thermocouples attached to the heater body itself, which means that the set point temperature for the heater body must be manually increased by steps until the desired sample temperature is obtained. The control software allows uploading of PID parameters specific to each experiment prior to heating for a shot. A test unit containing four dummy heater cells with thermocouples is used to test the control system between shots to ensure all components are in working order. Another pre-shot low-temperature test is performed with the control system hooked up to the experiment. Comparing the system's behavior between these two tests helps to troubleshoot wiring issues. The control unit now runs off two 30-amp 110-VAC circuits at Z for plenty of headroom when powering up to 16 heater cartridges. Isolation and toggle relays in the control unit have been upgraded to more robust components, which has decreased failure rates. The heater cartridges are fused individually with faster fuses than those used on the power supply, so that controlled heating can continue if a single heater shorts and fails.

Early experiments used ⅛" cartridge heaters, which commonly failed due to overheating as contact area decreased with thermal expansion of the copper heater body. The ¼" cartridge heaters used now include solid ceramic insulation on the individual power leads, are press fit into reamed ¼" holes in the heater body, and generally exhibit a high level of robustness despite the fact that they are not really intended for use in a vacuum environment.

2.2.2. Temperature Measurement

As mentioned in Section 2.1, temperature is measured using fine-gauge type-K thermocouples. Off-line tests comparing 75-μm and 25-μm leads indicated that the 75-μm leads are small enough relative to the sample size to avoid errors due to heat loss. Tests with thermocouples installed through the insulator from the power-flow surface (impossible to do for an actual experiment) showed that steady-state temperature varies less than 10 K between the center and edge of the sample.

Thermocouple materials are used in the wiring everywhere between the experiment and a Keithley® recording device, except for connections through the isolation relays. Since reference junction compensation is applied internally by the recorder, the non-thermocouple part of the circuit in the relays can introduce errors due to local thermal gradients within each relay. This error is not expected to be more than a few degrees, but has not actually been measured.

Some experiments showed large discrepancies between different thermocouples (TC's) located on the same sample. This was generally assumed to be an issue of thermal contact with the sample. When assembled correctly, the sample TC's typically read different temperatures upon initial heating, but then come to within 5-10 K of each other as the sample melts and wets the TC junctions. Discrepancies are thought to be due to one of two causes; either the sample holder is not seated properly

against the insulator, or the TC leads have shorted together some distance away from the sample. The first may be due to unequal thickness of the two insulators used with a dual-sample heater configuration. This issue has not yet been satisfactorily addressed. Solutions being considered include splitting the dual-sample heater body into two parts (that are still heated as one), spot-welding the TC's to the outside of the sample holder to measure its temperature instead, or installing the TC's through the sample housing prior to casting the sample to ensure good thermal contact.

Temperature measurements are sometimes required of the anode panel itself in order to analyze velocity measurements taken at other spots away from the tin samples. Early experiments relied on epoxy to attach TC beads to the panel, but these were found to often fail due to differential thermal expansion between the epoxy and the panel. All such measurements are now taken with the TC junction firmly clamped underneath the head of a #0-80 screw threaded into the panel material.

2.2.3. Thermal Insulation

It was desired to thermally insulate the liquid tin sample from the panels in order to reduce both the steady-state heat flow through the system and the panel temperature required for a given sample temperature. Since the compression wave must pass through the insulator to reach the sample, a material is needed with both high stiffness and low thermal conductivity. Unfortunately, such materials (typically ceramics) tend to have high elastic limits that adversely perturb the unsteady stress wave entering the molten tin. Early experiments attempted to use Pyroceram® 9608 glass ceramic which had previously been shown to exhibit anomalous compression (spreading instead of steepening a propagating wave) up to 20 GPa [Asay and Chhabildas, 1980]. Impact experiments carried out on three different batches of the material, however, showed this behavior to be very sensitive to microstructure, which itself is sensitive to small differences in ceramic processing. In particular, only one old batch of material (fabricated *c*. 1978 and used in the work of Asay and Chhabildas) had the superfine microstructure required to achieve anomalous compression to 20 GPa. Even in this case, a ramp wave propagated through the material takes on local disturbances which complicate analysis of subsequent propagation through liquid tin.

C-axis sapphire was chosen instead for later experiments because it can behave elastically up to 30 GPa under isentropic loading [Hall, 2003], and has a large longitudinal elastic modulus that is nearly linear in compression. Thus a ramped stress wave can propagate through several millimeters of sapphire with only minimal steepening. Unfortunately, sapphire has a relatively high thermal conductivity, approximately 40 W/m·K compared to 1-2 W/m·K for glass ceramics. The 2-mm thick sapphire insulators used on most of the liquid tin experiments typically support a temperature difference of 100 K under quasi-steady conditions. The pre-heat apparatus never truly reaches a steady-state temperature distribution because the power-flow structure at Z (to which the anode panels are attached) is made of stainless steel, which with its intermediate conductivity is both a poor thermal conductor and a poor thermal insulator. For a given sample temperature, the panels very slowly increase in temperature until the thermal gradient is supported entirely in the steel parts; normally, the experiment is over well before this would occur. A large copper heat sink was designed to attach to the tops of the panels and shown to significantly slow the increase in panel temperature.

In order to subject liquid tin samples to ramped compression waves of higher peak stress, the insulator must be removed from the path of the wave. Several designs to thermally insulate the power-flow surface beneath the sample from the rest of the anode panel were attempted on a few of the Z experiments. One such design is depicted in Figure 2-5. The annular insulator is coated on the power-flow surface with a copper layer 75 μm thick. One issue with this type of design is outward bowing of the cup insert under thermal stresses as it expands inside the rigid insulator, effectively increasing the thickness of the liquid sample. Finite-element analyses carried out by Bechtel Nevada indicate that bowing was significant (on the order of 50 μm increases in sample cell thickness) for earlier designs using threaded inserts, but was reduced to 1-2 μm by the design in Figure 2-5 which uses a floating cup insert with sliding contacts at the clamped lip and a radial gap of 50 μm inside the insulator. A second issue with these designs is disturbance of the uniform current flow on the anode,

possibly even shorting across the anode/cathode gap. Shot data suggest that annular insulators having a 2 mm exposed width do not cause a problem, but at 3 mm exposed width (as in Figure 2-5), the data are inconclusive. A better approach might be to eliminate the insulator altogether, but design the anode panel to allow relatively stress-free thermal expansion. More work is needed in this area for higher-pressure experiments that will further overdrive the solidification transition.

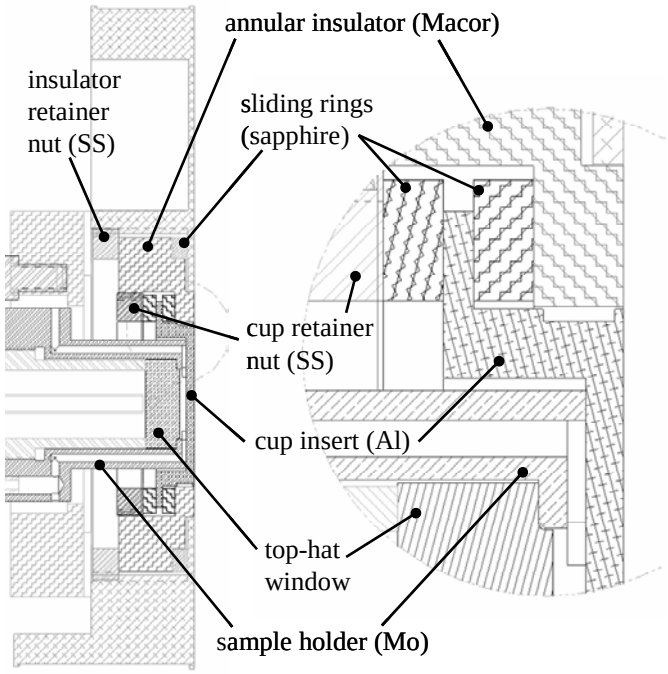

Figure 2-5: Cup insert design used on shot Z1064.

2.2.4. Sample Thickness

Analysis of VISAR data from isentropic compression experiments requires accurate knowledge of sample thickness. For liquid samples, the thickness of the confining sample cell must be known in the heated state. Early experiments used a one-piece sample holder with integrated lip (instead of a separate extension as in Figure 2-2) and relied upon pre-assembly measurements of the top-hat window step height and lip thickness to estimate sample cell thickness. VISAR results indicated that the actual sample was often significantly thicker than expected. To allow accurate machining of the inner surface of the lip and eliminate any radius at the inside corner, the sample holder design was changed to use a separate extension piece for the lip. Both sides of the extension could then be machined very flat and parallel. The first extension design used miniature screw fasteners, which failed to provide sufficient dimensional stability under thermal cycling. In the present design, the two parts are brazed together after they have been separately diamond-turned on both sides. Metrology is performed on the entire sample cell assembly, prior to casting a sample, to verify cell thickness and parallelism. Final sample thickness is computed from these numbers plus measurements taken after final machining, as well as estimated thermal expansion effects. Verification of this procedure by independent means, such as microscopy of a sectioned sample that has been remelted and cooled in a shot configuration, is planned but has not yet been undertaken.

As discussed in Section 2.2.3, further changes to liquid sample thickness can occur on experiments that do not use a sapphire insulator disc, due to bowing of the anode material underneath the sample.

2.2.5. Sample Purity

The earliest designs for liquid tin experiments failed to consider metal-metal reactions at elevated temperature and their effect on the composition of the liquid sample. For example, experiments prior to Fall 2002 used aluminum sample holders and stainless steel reservoir parts. During sample preparation, the assembly typically sat for at least half an hour at 575 K or higher temperature, which allowed the liquid tin to be saturated by up to 2% aluminum. Then the assembly was cooled very slowly, which allowed the aluminum to precipitate in nodules, discovered by back-scattered electron microscopy of a sectioned sample as shown in Figure 2-6. When such a sample is subsequently heated to a lower temperature for the experiment, some of the aluminum contamination would remain in solid form as the saturated liquid then contains less aluminum.

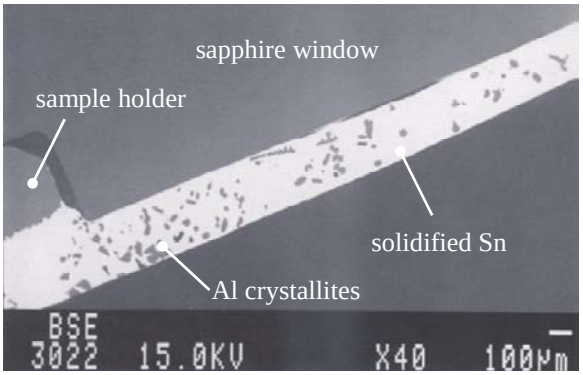

Figure 2-6: Back-scattered electron micrograph of sample assembly prepared for an early experiment, showing significant aluminum contamination.

The contamination issue was addressed by fabricating the sample holder of molybdenum (Mo), which does not react at all with tin under the relevant temperature range and yet has a thermal conductivity only 25% lower than aluminum. Later, the reservoir parts were also changed to Mo. In the current design, the only metals besides Mo with which the liquid tin comes in contact are the nickel coatings on the window and insulator, as described in Section 2.2.7. As received from the manufacturer, the tin used for injection casting of samples is 99.9985% pure. Plasma mass spectroscopy and electron microprobe analyses of processed tin samples indicate metal impurities on the order of 0.01-0.10% by mass**.** Figure 2-7 shows back-scattered electron micrographs of such a relatively high-purity sample. Higher purity is expected by improving cleanliness of the parts and the processes.

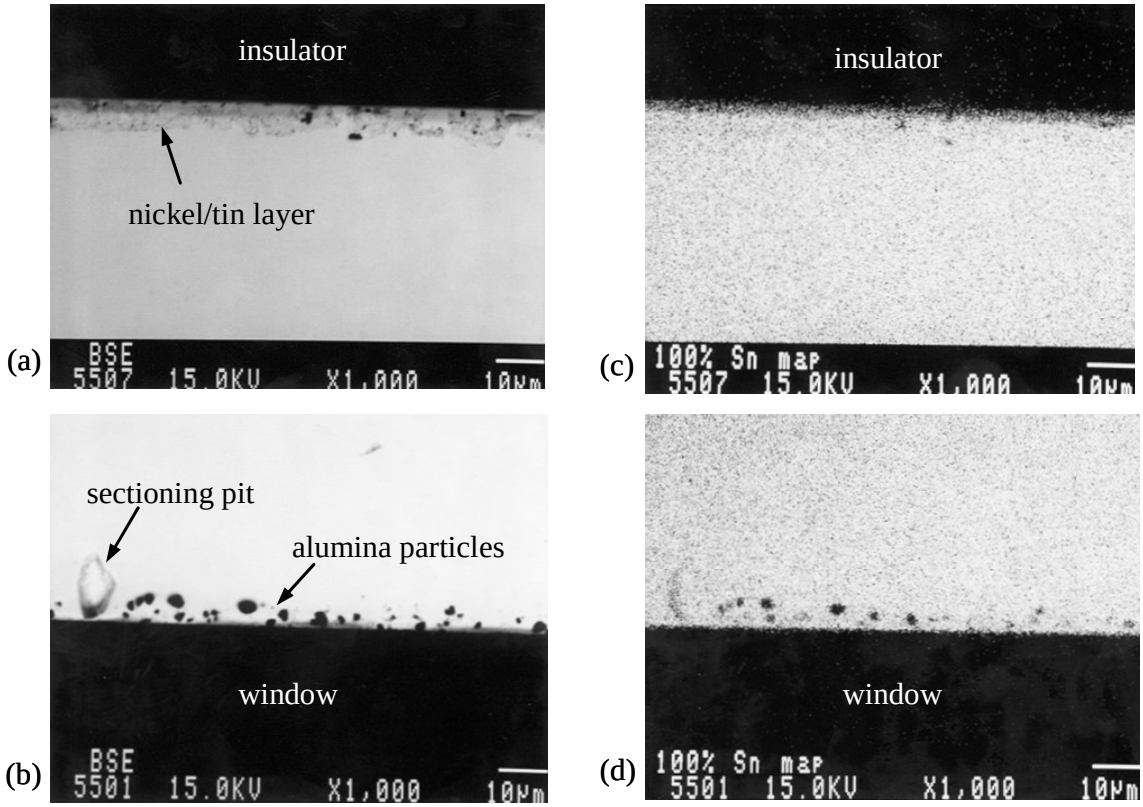

Figure 2-7: Back-scattered electron (a,b) and Sn-microprobe (c,d) micrographs of a resolidified, high-purity sample in two regions near the tin/insulator interface (a,c) and tin/window interface (b,d). It is not clear whether alumina particles were pre-existing or embedded by the sectioning and polishing process.

2.2.6. Sample Voids

Due to its high surface tension, liquid tin has a propensity to form voids within the sample cell during injection casting under vacuum, particularly next to non-reacting interfaces (such as the molybdenum sample holder). Any voids in the path of the propagating wave near the center of the

sample will perturb the velocity measurement at the window interface. Some of the early experiments were compromised in this way because they did not use any coating on the window. As described in Section 2.1, nickel films were found to be ideal to promote wetting by reacting with liquid tin without dissolving completely. Injection casting must be performed against an uncoated insulator, typically glass ceramic with just enough surface roughness to mechanically promote wetting. Since voids can commonly form against this insulator, the samples are cast thicker than needed, then diamond-tool machined to the desired thickness. The machining process may embed some sub-micron particles of molybdenum in the exposed tin surface, but this has yet to be investigated quantitatively. For an experiment, the machined tin surface is clamped against the nickel-coated sapphire insulator, and bonds to it upon heating to melt (see Figure 2-7a). Presently, all prepared samples are checked for hidden voids using X-ray radiography as shown in Figure 2-8. Occasionally, a sample has been found to have voids near the window (Figure 2.8b). The problem has tentatively been blamed on cleanliness and thin-film deposition issues, but more work is needed verify this.

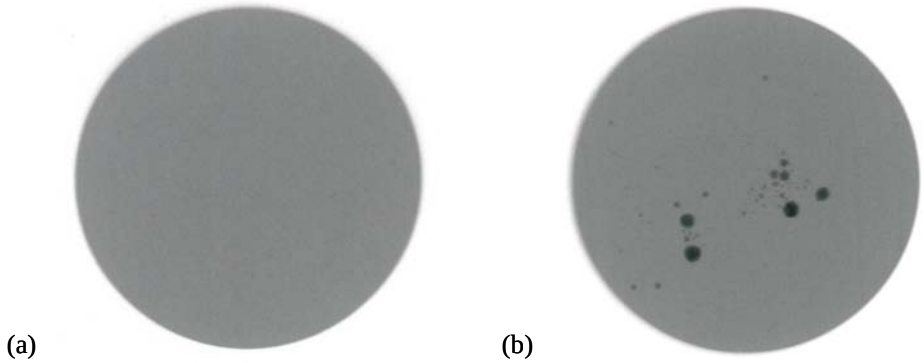

Figure 2-8: Negative X-Ray radiographs of two prepared tin samples, one without voids (a) and one with voids (b). Darker areas correspond to lower integrated density along the axial direction, and the circular field of view covers the central 3 mm of each sample.

2.2.7. Window and Insulator Coatings

The VISAR measurements require a film coating on the window at the window/sample interface that is highly reflective at a 532-nm wavelength. For reasons described in Sections 2.1 and 2.2.6, a nickel film is required adjacent to the liquid tin. These coatings must remain adhered to the window substrate during heating to above 600 K in a vacuum prior to injection casting of the sample, cooling back to room temperature, and subsequent reheating for the experiment. This last requirement was particularly difficult to meet for LiF windows due to differential thermal expansion. Some early experiments used a silver reflector, but aluminum was found to have the best combination of adhesion to both LiF and sapphire with high reflectivity (approximately 90% at 532 nm). A number of experiments used a chromium adhesion layer between the aluminum and the substrate; unfortunately, this greatly reduced VISAR signal intensities because chromium is highly absorbent at 532-nm wavelength. Nickel deposited directly on the aluminum film was found to react with the aluminum and reduce its reflectivity at elevated temperatures.

The only coating scheme discovered to date that meets the above requirements consists of a 500-nm aluminum reflector followed by a 20-nm titanium nitride barrier layer, a 20-nm titanium adhesion layer, and a 300-nm nickel wetting layer, all sputter-deposited under a 5-mtorr atmosphere of argon. In order to reduce the maximum thermal strain during the sample preparation procedure, the LiF substrates are pre-heated to at least 425 K prior to deposition. This coating scheme has been shown to survive multiple heating cycles, maintain good reflectivity, and produce void-free wetting of the liquid tin.

2.2.8. High-Temperature VISAR Probes

Standard bare-fiber VISAR probes used on room-temperature experiments at Z consist of four 200-µm-core silica fibers with polyamide buffer coating, potted inside a close-fitting stainless steel hypodermic needle with slow-cure epoxy. A high-temperature version of this probe must use materials with thermal expansion similar to silica that do not pyrolize nor significantly evaporate when heated under vacuum. After several iterations, the design for this probe has settled on use of a long ceramic tube of nominally 1.5-mm inner diameter, with a smaller ceramic tube (0.6-mm inner diameter) insert at one end. The fibers are bundled together and potted into the center of the insert using Aremco® Ceramabond high-temperature adhesive #671, which is based on very fine-grained alumina powder. The opposite end of the outer tube where the fibers exit the probe is potted with a slow-curing epoxy and vented with a small length of stainless steel tubing. The polyamide buffer material does evaporate to some extent when heated in vacuum, and caused up to a 50% decrease in signal return on earlier experiments. The probes now use fiber with a different color buffer having lower absorption at 532-nm wavelength, and they are pre-processed by heating under vacuum to evaporate some of the buffer prior to installation on the experiment. Measurements under heated conditions indicate probe efficiencies around 1-3% when used with 3-mm thick windows. Figure 2-9 is a micrograph of the bare fiber ends potted in the high-temperature adhesive.

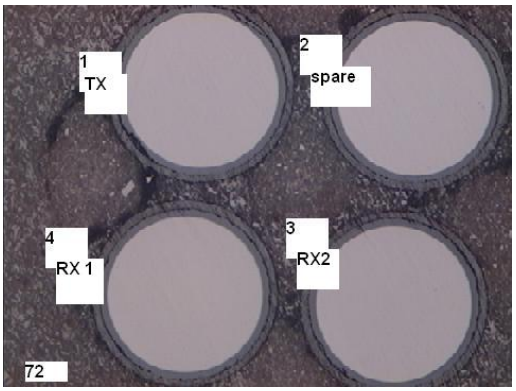

Figure 2-9: Micrograph of high-temperature VISAR probe showing 200-µm-core fibers embedded in alumina-based adhesive

A different probe issue was discovered and resolved during off-line probe testing under heated conditions. The threaded probe nut used at the back of the heater body to position the probe was originally made of Macor® ceramic, and had a tendency to break at the shoulder due to tension from thermal expansion of the mating copper threads. This may have been the reason for loss of VISAR signals on a number of shots. The current design uses a stainless steel probe nut as shown in Figure 2-2.

2.2.9. High-Temperature Bonds

Bond layers are used between solid materials in the path of the propagating compression wave in order to hold the parts together during handling and to ensure a void-free mechanical contact. Even micron-scale voids can cause low-level shock formation at the foot of a ramped wave. For pre-heat experiments, these bonds are used between the insulator and the anode panel, and between materials used to make a drive measurement (for example, an insulator and a window without a tin sample). Opening of voids inside the bond layers due to thermal stresses under heating has proven to be a serious issue for experiments on liquid tin. The differential thermal expansion between sapphire and aluminum or copper is significant. Early experiments used standard 30-minute epoxy, which very commonly resulted in velocity measurements that exhibit partial shocking. Stycast® #1266 epoxy was found to work fairly well because it remains slightly flexible after curing, and has been used for many of the experiments. But even this adhesive resulted in partially shocked ramp waves at least 20% of the time. Heating tests were performed using uncoated sapphire substrates to allow characterization of the bond layer's appearance; these showed a small number of voids, on the order of 10 µm in size) appearing in the Stycast® epoxy after one heating/cooling cycle. Silicone gels were shown in other heating tests to eliminate voids, but have unacceptably high thermal expansion.

Development has begun on the use of indium layers that become liquid when heated and thus allow for large differential thermal expansions without forming voids. The layer of course no longer acts as an adhesive once melted, but the parts being bonded are typically clamped together prior to

heating (see Figure 2-2). A bonding process based on the work of So and Lee (2000) has shown some success, but needs further testing. The best approach may be to avoid the issue altogether by eliminating the insulator from the path of the propagating wave, as discussed in Section 2.2.3.

2.2.10. Current-Pulse Shaping

The shape of the pulse of current driving the ramp-wave compression can have a profound effect on the outcome of an experiment. The pulse must have a shape that allows shockless propagation through the liquid sample, and liquids have rather non-linear compression behavior compared to solids. In addition, the pulse shape must not allow high current to burn through the full thickness of the anode plate until after the stress wave has traversed the insulator and the sample. Otherwise, plasma jetting around the sides of the insulator may be able to close a circuit through the sample holder, joule-heating the sample prior to arrival of the stress wave.

The earliest experiments were performed on the Saturn accelerator with a fixed pulse shape. The first experiments performed on Z also used a fixed pulse shape of shorter rise-time than Saturn; the data from these suggest the samples were pre-vaporized by joule heating. The next several experiments used high-inductance mode on the Z machine, which significantly spreads out the pulse shape, along with pre-firing of ¼ of the machine to spread the foot of the pulse even more. This type of pulse produced some nice data, but was unhealthy for the Z machine and significantly limited the peak pressure that could be obtained. With the advent of more precise control of pulse shaping on Z [Davis *et al*, 2005], some attempts were made to achieve higher pressure without high-inductance mode, while maintaining a pulse shape similar to the computed ideal shape and staying below 30 GPa in the sapphire insulator. Some of the data suggest the computed ideal pulse shape is not accurate, with shock formation occurring more quickly than expected in the liquid. A better approach may be to spread the pulse out as much as possible while still producing the desired peak pressure.

2.2.11. Summary of Design Status

While many of the problems encountered during development of the pre-heat system have been addressed, the ultimate goal of an experiment providing repeatable, high-quality data has yet to be realized. The main issues that remain to be solved are those of high-temperature bonds (Section 2.2.9) and consistent temperature measurement (Section 2.2.2). These issues could be circumvented on the next experiment by revisiting the no-insulator design discussed in Section 2.2.3 and applying more recent lessons learned regarding coatings, probes, and pulse shape.

3. EXPERIMENTAL RESULTS

Measurement results from the isentropic compression experiments on liquid tin consist of VISAR velocity histories, properly timed relative to one another and taken at known spatial locations. While some qualitative observations can be made from these, a full understanding of their significance can only come from careful analysis of the experiments, usually using a wave propagation code of some kind. In the interest of complete documentation, Section 3.1 presents data collected from every experiment on liquid tin, even those performed prior to the start of the present LDRD. A preliminary analysis of some of these data is given in Section 3.2.

3.1. VISAR Measurements

Data are presented here in chronological order for every experiment on molten tin that has been performed at the Saturn and Z machines, starting in May 2001. For each shot, a graph shows relevant velocity curves and a table gives detailed information on materials, layer thicknesses, and temperatures at each measurement location. Numbers in parentheses are nominal, estimated, or average values, indicating either that more precise information is not available or, in the case of some temperatures cited, the measurements exhibited exceptionally large scatter. The text describes design changes relative to the previous shot, qualitative observations, and problems encountered. The phrase "drive measurement" refers to velocity measurements taken without a sample. Peak drive pressure is maximum longitudinal stress in the material layer that immediately precedes the liquid tin, whether this be an insulator or anode panel. Each velocity measurement is labeled by its location on the load. Many of the velocity curves are cut off fairly early in time due to loss of signal when the wave, which has steepened considerably while traversing the liquid tin, forms a shock in the sapphire window.

S-2925	North Bottom	North Top	South
Panel	Aluminum (0.6 mm)	Aluminum (0.6 mm)	Aluminum (0.6 mm)
Insulator	New Pyrocer. (2.0 mm)	New Pyrocer. (2.0 mm)	New Pyrocer. (2.0 mm)
Sample	(0.4 mm) (600 K)	(0.7 mm) (600 K)	none (600 K)
Window	Sapphire (2.0 mm)	Sapphire (1.7 mm)	Sapphire (2.0 mm)
Peak Drive Pressure = 22 GPa Split window with silver coating Integrated copper sample holder / heater body			

Table 3-1: Saturn shot 2925

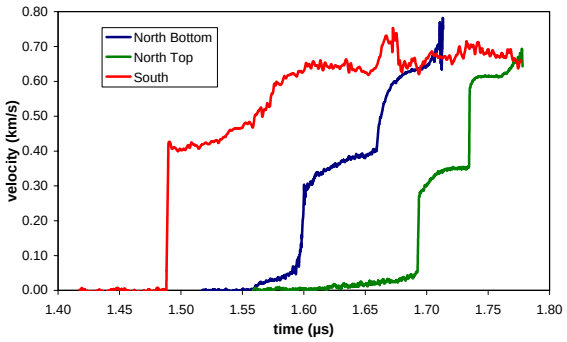

Figure 3-1: Saturn shot 2925

Saturn Shot 2925

This shot (and the next three) were performed at the Saturn accelerator as part of a LDRD project to demonstrate Saturn as a platform for ICE [Furnish *et al*, 2001]. A two-panel rectangular load was used to obtain > 20 GPa because Saturn produces only 10 MA of peak current. One panel had a single stepped tin sample, the other had a heated insulator without tin. The stepped sample was formed by a split (two-part) window having two step heights. The sample was cast in place (not by injection), leading to large uncertainty in sample thickness. "New" Pyroceram® was produced in a small batch by the Corning Cells Group in 2001 (Pyroceram® 9608 is no longer commercially available). The drive measurement (South) suggests a compromised bond layer, probably between the aluminum and ceramic. The two-wave structure emanating from the tin sample has almost certainly been transmitted from the insulator, and is not due to any processes occurring in the tin. The sample

also would have been highly contaminated by copper. The integrated sample holder and heater body was made of copper and held up to eight miniature cartridge heaters.

S-2926	North Bottom	North Top	South Bottom
Panel	Aluminum (0.6 mm)	Aluminum (0.6 mm)	Aluminum (0.6 mm)
Insulator	New Pyrocer. (2.0 mm)	New Pyrocer. (2.0 mm)	New Pyrocer. (2.0 mm)
Sample	(0.4 mm) (700 K)	(0.7 mm) (700 K)	None (700 K)
Window	Sapphire (2.3 mm)	Sapphire (2.0 mm)	Sapphire (2.0 mm)
Peak Drive Pressure = 16 GPa Split window with silver coating Integrated copper sample holder / heater body			

Table 3-2: Saturn shot 2926

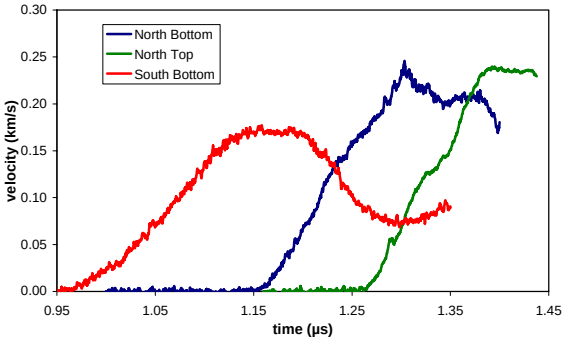

Figure 3-2: Saturn shot 2926

Saturn Shot 2926

Except for the use of a four-panel square load to obtain lower peak pressure, this shot was the same as the previous one. (The other two panels held non-heated experiments.) It appears to exhibit some asymmetry in loading between the panels that was a common problem on Saturn shots due to load alignment issues. It is not clear whether the wave profile shape for North Top (NT), *i.e.*, the slight plateau at 0.13 km/s, is due to behavior of the insulator or the molten tin.

S-2969	North Middle	North Top	South Top
Panel	Copper (0.4 mm)	Copper (0.4 mm)	Copper (0.4 mm)
Insulator	Old Pyroceram (2.0 mm)	Old Pyroceram (2.0 mm)	Old Pyroceram (2.0 mm)
Sample	(0.45 mm) (600 K)	(0.24 mm) (600 K)	None (350 K)
Window	LiF (1.8 mm)	LiF (2.0 mm)	LiF (3.0 mm)
Peak Drive Pressure = 10 GPa Split window without coating Separate aluminum sample holder threaded onto heater body			

Table 3-3: Saturn shot 2969

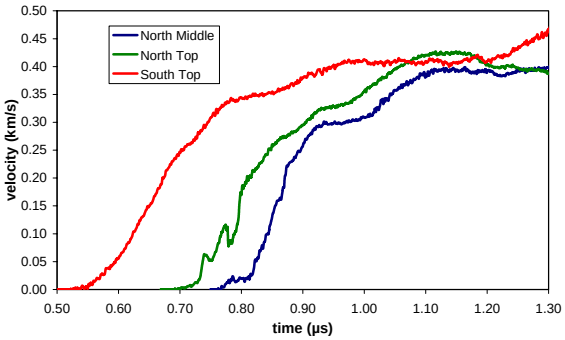

Figure 3-3: Saturn shot 2969

Saturn Shot 2969

Changes for this shot include a separate aluminum sample holder, Pyroceram® material from an old batch, and a LiF split window without any coating; the molten tin itself served as a (poor) reflector. The North Top (NT) velocity perturbations are probably due to voids at the window interface positioned laterally from the VISAR measurement spot. Equilibrium solidification would produce a signature in the velocity profile at about 0.3 km/s, where the measurements show a slight plateau.

Saturn Shot 2970

This shot returned to a two-panel rectangular load configuration for higher pressure, but was otherwise identical to the previous shot. The plateau at 0.3 km/s again corresponds nicely with entry into the mixed-phase region for an equilibrium solidification transition. Both measurements then level off at about 0.5 km/s, much lower than expected for the given peak pressure in the South panel. The late-time rise cannot be attributed to reflections or edge effects, suggesting that it is due to behavior of the tin itself. The foot of the North Middle (NM) profile was compromised by interferometer beam-path crosstalk and is not shown. The foot of the North Top (NT) profile exhibits a precursor with a magnitude corresponding to an extrapolation of the β–γ solid–solid phase co-existence curve

S-2970	North Middle	North Top	South Top
Panel	Copper (0.4 mm)	Copper (0.4 mm)	Copper (0.4 mm)
Insulator	Old Pyroceram (2.0 mm)	Old Pyroceram (2.0 mm)	Old Pyroceram (2.0 mm)
Sample	(0.36 mm) (600 K)	(0.56 mm) (600 K)	None (350 K)
Window	LiF (1.8 mm)	LiF (2.0 mm)	LiF (3.0 mm)
Peak Drive Pressure = 25 GPa Split window without coating Separate aluminum sample holder threaded onto heater body			

Table 3-4: Saturn shot 2970

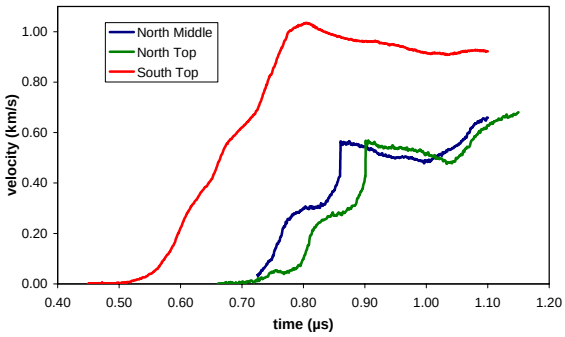

Figure 3-4: Saturn shot 2970

beyond the triple point into the liquid region, suggesting a possible liquid–liquid transition. Based on this experiment, one purpose of the original LDRD project was to determine if tin could exhibit such a transition. Later characterization of prepared tin samples indicated the presence of solid aluminum crystallites (see Section 2.2.5), a far more likely explanation for the precursor.

Z Shot 902

This first shot on Z was also the first to use single-piece top-hat windows (single thickness per sample), injection casting for sample preparation, taller panels allowing a drive measurement on each panel, and machined grooves on the insulator to mount thermocouples in contact with the sample itself. The load had four panels, but only two were used for pre-heated tin. The two separate drive measurements clearly show the irreproducibility of the Pyroceram® insulator material. The waves emanating from both tin samples arrived much later than expected, even later than can be reasonably explained by uncertainty in the sample thickness. This may be due to the shorter rise-time current pulse on Z compared to Saturn; if magnetic field diffused through the anode plate prior to arrival of the compression wave at sample/window interface, then jetting of anode material around the insulator could have completed a circuit through the sample, pre-heating it even to a vapor state.

Z-902	North Top	North Bottom	South Top	South Bottom
Panel	Aluminum 0.611 mm	Aluminum 0.613 mm	Aluminum 0.608 mm	Aluminum 0.611 mm
Insulator	Old Pyroceram 2.068 mm	Old Pyroceram (2.0 mm)	Old Pyroceram 2.070 mm	Old Pyroceram (2.0 mm)
Sample	none (325 K)	(0.24 mm) 545 K	none (350 K)	(0.46 mm) 560 K
Window	LiF (3.0 mm)	Sapphire (3.0 mm)	LiF (3.0 mm)	Sapphire (3.0 mm)
Peak Drive Pressure = 19 GPa Aluminum coating on windows Separate aluminum sample holder bolted onto heater body				

Table 3-5: Z shot 902

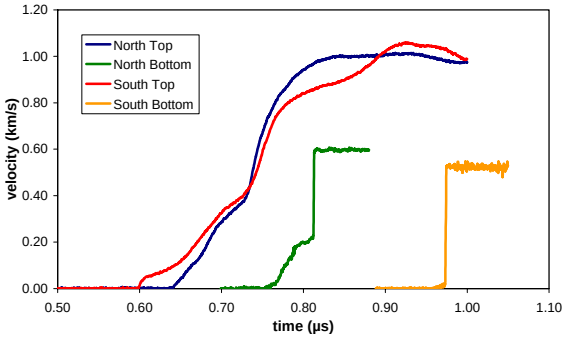

Figure 3-5: Z shot 902

Z Shot 903

Identical to Z Shot 902, this shot suffered the same problems. In addition, the North panel data were lost due to probe and VISAR issues. The Pyroceram® insulator produces a wave profile that is again different from either of those measured on the previous shot.

Z Shot 938

For this and subsequent shots, the machine was set up in high-inductance mode, sometimes with a pre-pulse on nine feed lines, to spread out the pulse. This also lowers the peak pressure. The insu-

lators were made from a different old batch of Pyroceram®, darker in color and with finer microstructure. Unfortunately, the data on liquid tin were compromised by probe and/or VISAR issues.

Z-903	South Top	South Bottom	
Panel	Aluminum 0.610 mm	Aluminum (0.6 mm)	
Insulator	Old Pyroceram 2.071 mm	Old Pyroceram (2.0 mm)	
Sample	none (325 K)	(0.45 mm) 575 K	
Window	LiF (3.0 mm)	Sapphire (3.0 mm)	
Peak Drive Pressure = 19 GPa Aluminum coating on windows Separate aluminum sample holder bolted onto heater body			

Table 3-6: Z shot 903

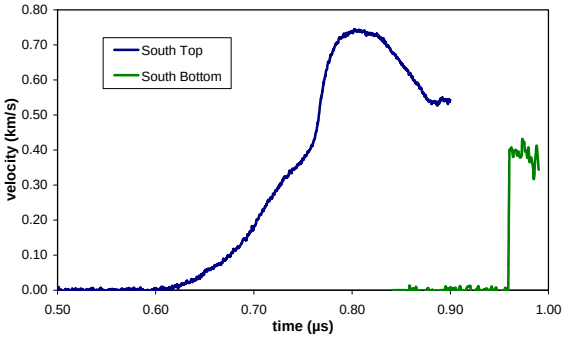

Figure 3-6: Z shot 903

Z-938	South Bottom	South Top	North Top
Panel	Aluminum 0.609 mm	Aluminum 0.610 mm	Aluminum 0.610 mm
Insulator	Old Pyroceram 2.044 mm	Old Pyroceram 2.005 mm	Old Pyroceram 2.005 mm
Sample	(0.50 mm) (570 K)	none (325 K)	none (325 K)
Window	Sapphire (3.0 mm)	LiF (3.0 mm)	LiF (3.0 mm)
Peak Drive Pressure = 11 GPa Aluminum coating on windows Separate aluminum sample holder bolted onto heater body			

Table 3-7: Z shot 938

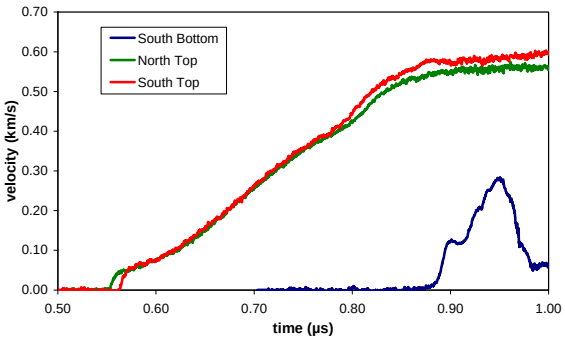

Figure 3-7: Z shot 938

Z Shot 964

This shot was the first to use a molybdenum sample holder, to eliminate the ⅛" cartridge heaters in favor of a band heater, and to use four independently controlled heater cells. Other changes include nickel coatings on the top-hat windows and a threaded Macor® probe holder. This particular shot had no insulators, instead using a threaded aluminum cup insert insulated from the rest of the panel by a threaded Macor® ring (a predecessor to the design in Figure 2-5). The design successfully eliminated insulator issues, but the resulting data suggest that the sample thickness was on the order of 35-60 µm higher than measured (see Section 3.2.3). Later finite-element studies indicate that increases in sample cell thickness of 50-60 µm can occur due to bowing of the cup insert at high temperatures. Only the East Bottom (EB) sample shows possible evidence of solidification. For the South Bottom (SB) sample, the ramp wave has steepened into a shock. The molybdenum sample holder eliminated aluminum contamination, but characterization of similarly-prepared samples still showed about 0.2% impurities from the stainless-steel injection hardware.

Z-964	North Top-2	North Bottom	East Bottom	South Bottom
Panel	Aluminum 0.608 mm	Aluminum 0.610 mm	Aluminum 0.611 mm	Aluminum 0.613 mm
Insulator	none	none	none	none
Sample	none 410 K	(0.34 mm) 575 K	(0.50 mm) 720 K	(0.71 mm) 625 K
Window	LiF (3.0 mm)	Sapphire (3.0 mm)	Sapphire (3.0 mm)	Sapphire (3.0 mm)
Peak Drive Pressure = 13 GPa Nickel coating on windows Separate molybdenum sample holder bolted onto heater body				

Table 3-8: Z shot 964

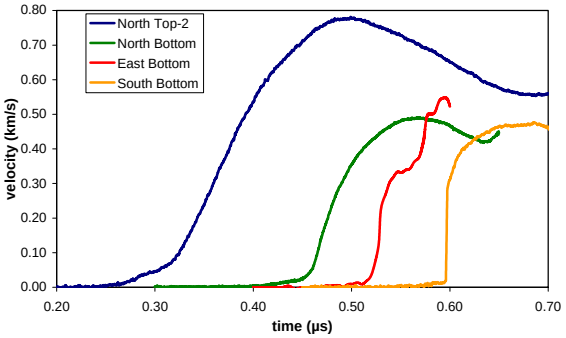

Figure 3-8: Z shot 964

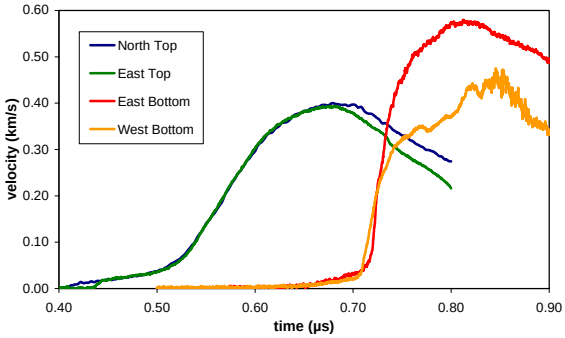

Figure 3-9: Z shot 965

Z Shot 965

This shot was similar to the previous except for the use of TC-instrumented sapphire insulators (Pyroceram® was abandoned after Z shot 938). Sapphire made the drive measurements more repeatable, but also clearly showed the unpredictable effect of thermal stresses on the glue bonds, as seen at the foot of the North Top (NT) and East Top (ET) measurements. Late-time drive data were compromised by motion of the window's back surface. Some data were lost on this shot due to probe and VISAR issues. The data do not exhibit any clear signature attributable to solidification.

Z-965	North Top	East Top	East Bottom	West Bottom
Panel	Aluminum 0.820 mm	Aluminum 0.812 mm	Aluminum 0.812 mm	Aluminum 0.810 mm
Insulator	Sapphire 2.197 mm	Sapphire 2.164 mm	Sapphire 2.119 mm	Sapphire 2.179 mm
Sample	none (400 K)	none (400 K)	(0.556 mm) 550 K	(0.509 mm) 550 K
Window	Sapphire 3.212 mm	Sapphire 3.218 mm	LiF (3.0 mm)	Sapphire (3.0 mm)
Peak Drive Pressure = 18 GPa Nickel coating on windows Separate molybdenum sample holder bolted onto heater body				

Table 3-9: Z shot 965

Z Shot 1007

Essentially identical to the previous shot, this shot unfortunately experienced problems with heater control that left two samples (data not shown) in solid form. Drive measurements again displayed variability at the foot of the wave profile. The East Bottom (EB) sample has shocked, suggesting either a large gap underneath the insulator or a thicker sample than expected.

Z-1007	North Top	North Bottom	East Bottom
Panel	Aluminum 0.818 mm	Aluminum 0.812 mm	Aluminum 0.814 mm
Insulator	Sapphire 2.168 mm	Sapphire 2.194 mm	Sapphire 2.192 mm
Sample	none (450 K)	(0.341 mm) 650 K	(0.509 mm) (650 K)
Window	Sapphire (3.0 mm)	Sapphire (3.0 mm)	Sapphire (3.0 mm)
Peak Drive Pressure = 20 GPa Nickel coating on windows Separate molybdenum sample holder bolted onto heater body			

Table 3-10: Z shot 1007

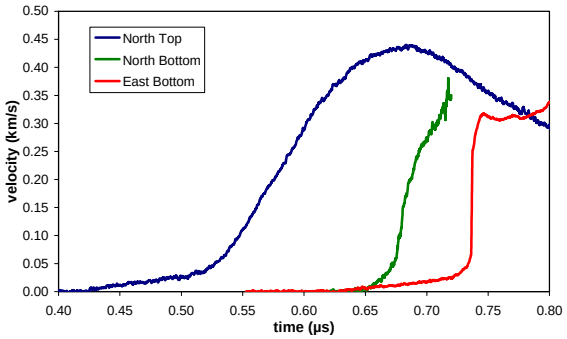

Figure 3-10: Z shot 1007

Z Shot 1008

The only difference between this shot and the previous was a change to 4-mm thick sapphire windows for the drive measurements. One of the four drive measurements (not shown) had a shocked

foot, evidence of a compromised glue bond. All four samples were successfully heated to the liquid state and returned reasonable VISAR data. The wave arrival time and shock for West Bottom (WB) indicate that this sample was considerably thicker than measured (this wave should have arrived earlier than South Bottom). There is no obvious signature of solidification in these data.

Z-1008	North Top	East Bottom	North Bottom	South Bottom	West Bottom
Panel	Aluminum 0.811 mm	Aluminum 0.813 mm	Aluminum 0.814 mm	Aluminum 0.809 mm	Aluminum 0.809 mm
Insulator	Sapphire 2.016 mm	Sapphire 2.010 mm	Sapphire 2.142 mm	Sapphire 2.170 mm	Sapphire 2.019 mm
Sample	none (450 K)	(0.344 mm) 600 K	(0.351 mm) 530 K	(0.554 mm) 545 K	(0.564 mm) 635 K
Window	Sapphire 4.014 mm	Sapphire (3.0 mm)	Sapphire (3.0 mm)	Sapphire (3.0 mm)	Sapphire (3.0 mm)
Peak Drive Pressure = 19 GPa Nickel coating on windows Separate molybdenum sample holder bolted onto heater body					

Table 3-11: Z shot 1008

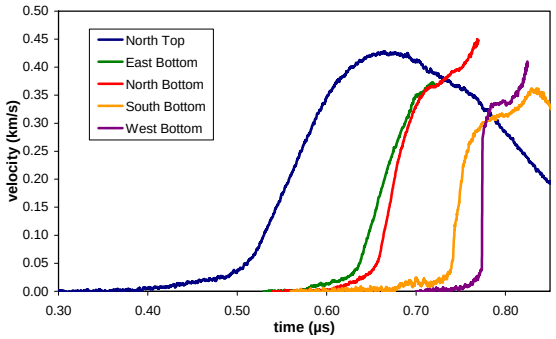

Figure 3-11: Z shot 1008

Z Shot 1064

This shot used the cup insert design shown in Figure 2-5 to eliminate insulators. It was also the first shot on Z to use a two-panel rectangular load configuration, with two heater cells per panel, to achieve somewhat higher pressure. This and the next two shots used a new window coating scheme to mitigate delamination from LiF substrates during sample preparation. The aluminum layer has a coefficient of thermal expansion intermediate between LiF and nickel, and is also more reflective than nickel. The chromium adhesion layer, however, significantly reduced reflectivity. The drive measurements taken at the center of each panel indicate some panel-to-panel variation of the current pulse; it is not clear whether this is due to power-flow issues with the insulated-cup design or simple misalignment of the anode and cathode. A new capability to shape the current pulse at Z was used to avoid high-inductance mode (which can cause damage to the machine). Unfortunately, the resulting pulse shape was far from ideal, causing three of the four samples to shock up completely (only North Bottom is shown here). The cause of the disturbance in the South Bottom (SB) velocity profile at 0.75 km/s is unknown.

Z-1064	North Center	South Center	North Bottom	South Bottom
Panel	Aluminum 0.812 mm	Aluminum 0.812 mm	Aluminum (0.8 mm)	Aluminum (0.8 mm)
Insulator	none	none	none	none
Sample	none 380 K	none 380 K	(0.655 mm) 555 K	(0.335 mm) 545 K
Window	LiF (3.0 mm)	LiF (3.0 mm)	LiF (3.0 mm)	LiF (3.0 mm)
Peak Drive Pressure = 18 GPa Window coatings (sputtered) = Cr adhesion + Al + Ni Separate molybdenum sample holder bolted onto heater body				

Table 3-12: Z shot 1064

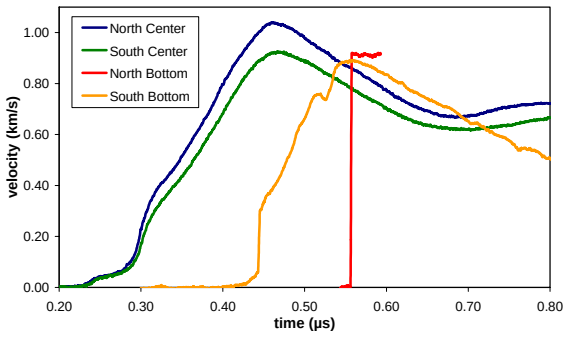

Figure 3-12: Z shot 1064

Z Shot 1181

The design was changed for this shot to use dual-sample heaters, allowing up to 8 samples to

be heated by four heater cells on four panels. The larger heater body incorporated one band heater and two ¼" cartridge heaters, and injection casting began to use all molybdenum parts. Another significant change was to split the sample holder into two parts, with the lip incorporated into an extension part that could be machined flat and parallel on both sides while also eliminating any internal radius on the surface that mates to the top-hat window. This shot used screws to attach the extension to the rest of the sample holder, which turned out to cause very poor dimensional stability under heating for sample preparation. Pulse shaping was used again, but with part of the machine in high-inductance mode to ensure low ramping rate at the pulse foot. The drive measurements consisted of anode free-surface velocities, and the anode was made thicker to ensure these were not compromised by wave reverberation. No data on liquid tin were obtained from this shot, due to a combination of issues with probes and windows (low light return), VISAR setup (crosstalk between channels), and sample thickness or pulse shape (many samples entirely shocked).

Z-1181	North Center	East Center	
Panel	Aluminum (1.2 mm)	Aluminum (1.2 mm)	
Insulator	none	none	
Sample	none (560 K)	none (560 K)	
Window	None	None	
Peak Drive Pressure = 17 GPa Window coatings (sputtered): Cr adhesion + Al + Ni (LiF), Cr adhesion + Ni (Sapphire) Two-part molybdenum sample holder, extension bolted on			

Table 3-13: Z shot 1181

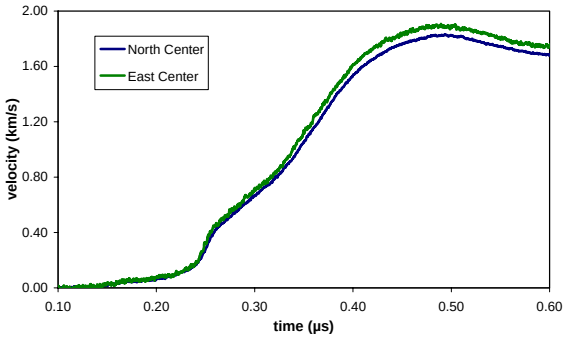

Figure 3-13: Z shot 1181

Z Shot 1273

For this shot, the sample holder extension was brazed to the rest of the sample holder, which gave high dimensional stability and parallelness. The square anode/cathode size was reduced to obtain higher pressure while using high-inductance mode. The pulse shape incorporated 28 high-inductance lines on Z, many more than the previous shot. Uniform temperatures were obtained by using matched-thickness insulators within each panel and placing a Macor® insulator underneath the panel assembly. Improvements were made to the metrology process to characterize the sample cell thickness. This shot was the first to use stainless-steel probe nuts. The drive measurements indicate a very asymmetric current pulse (East Center and West Center, not shown, mimic North Center and South Center, respectively). This was probably due to a design change in the cathode assembly that was intended to improve alignment. The data for North Top (NT) and North Bottom (NB) sug-

Z-1273	North Center	South Center	North Top	North Bottom
Panel	Aluminum 1.221 mm	Aluminum 1.212 mm	Aluminum 1.219 mm	Aluminum 1.221 mm
Insulator	none	none	Sapphire 1.998 mm	Sapphire 1.999 mm
Sample	none 540 K	none 540 K	(0.372 mm) 550 K	(0.495 mm) 555 K
Window	Sapphire 4.126 mm	Sapphire 4.119 mm	Sapphire (3.0 mm)	Sapphire (3.0 mm)
Peak Drive Pressure = 13 GPa (in aluminum) Window coatings (sputtered): Cr adhesion + nickel (Sapphire) Two-part molybdenum sample holder, extension brazed on				

Table 3-14: Z shot 1273

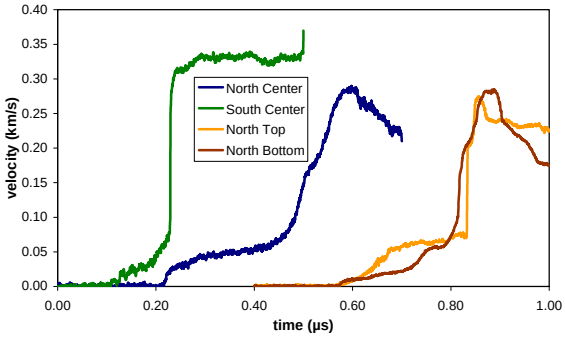

Figure 3-14: Z shot 1273

Z-1476	East Center	East Top	East Bottom	North Center	North Top	South Center	South Bottom	West Center	West Top
Panel	Copper 0.754 mm	Copper 0.753 mm	Copper 0.749 mm	Copper 0.764 mm	Copper 0.765 mm	Copper 0.766 mm	Copper 0.768 mm	Copper 0.752 mm	Copper 0.752 mm
Insulator	Sapphire 1.961 mm	Sapphire 2.045 mm	Sapphire 2.032 mm	Sapphire 1.960 mm	Sapphire 2.036 mm	Sapphire 1.992 mm	Sapphire 2.039 mm	Sapphire 1.960 mm	Sapphire 2.021 mm
Sample	none 525 K	0.497 mm 575 K	0.494 mm 560 K	none 525 K	0.621 mm 530 K	none 525 K	0.419 mm 565 K	none 525 K	0.331 mm 575 K
Window	Sapphire 3.394 mm	LiF 3.157 mm	Sapphire 3.099 mm	Sapphire 3.416 mm	Sapphire 3.103 mm	Sapphire 3.413 mm	Sapphire 3.098 mm	Sapphire 3.411 mm	LiF 3.146 mm
Peak Drive Pressure = 25 GPa Window coatings (sputtered): Al + TiN barrier + Ti adhesion + Ni (LiF), Ag + Ni (Sapphire) Two-part molybdenum sample holder, extension brazed on									

Table 3-15: Z Shot 1476

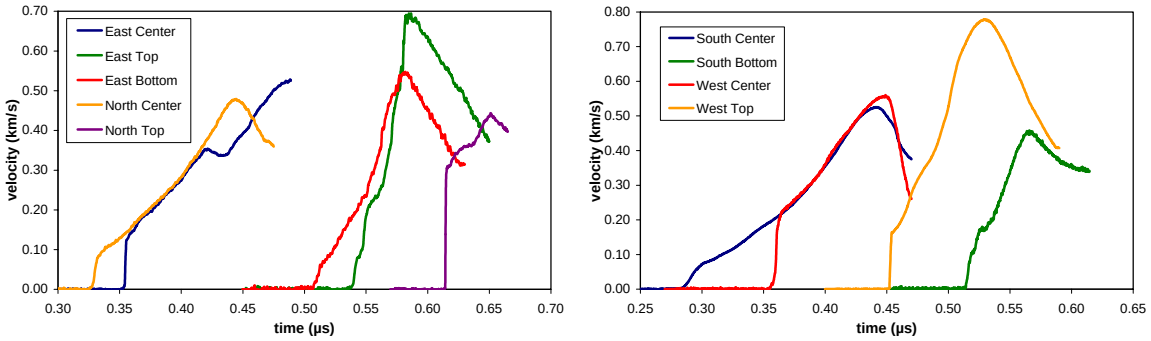

Figure 13-15: Z Shot 1476

gest that the driving current may have been nonuniform even within each panel. Very low light levels prevented useful data from any of the remaining six samples.

Z Shot 1476

This shot made use of further advances in pulse shaping to obtain a long rise-time current without resorting to high-inductance mode. To keep the peak pressure below the elastic limit of sapphire, the anode/cathode configuration was designed to a new intermediate size. A new coating scheme for the windows eliminated any absorptive adhesion layer on the substrate and avoided aluminum-nickel reactions with a titanium nitride barrier layer. To save space, the heater body was redesigned to use four cartridge heaters and no band heater. Probe stand-off clamps were added to precisely set the distance between probe end and window. Insulators were used above and below the anode panel assembly to maintain a more uniform temperature. This shot was also the first to make use of indium bonds between the insulators and the panel. The process was only successful in three locations (North Bottom, East Bottom, and West Bottom), and the remaining insulators were bonded using Stycast® #1266 epoxy, as were the insulators and windows at the center drive measurement locations. Three out of the four drive measurements indicate a compromised glue bond, which is likely to have occurred for several of the samples as well (North Top and West Top, for example). The indium bond at East Bottom (EB) appears to have prevented shock formation. X-ray radiography of cast tin samples was begun for this shot; only one sample had significant voids (Figure 2-8b), and it was not used on the shot. The data in Figure 13-15 are split into two graphs according to VISAR system; accurate cross-timing information between the two systems is not available at this writing. Some data were lost to problems with one of the VISAR systems, and some data were lost to shocked-up samples.

Z Shot 1541

This last shot performed during the LDRD project had only two panels with liquid samples. Because the other two panels were intended to see lower temperature (for heated solid samples), the de-

Z-1541	North Center	North Top	North Bottom	South Center	South Top	South Bottom
Panel	Copper 0.749 mm	Copper 0.756 mm	Copper 0.747 mm	Copper 0.755 mm	Copper 0.754 mm	Copper 0.756 mm
Insulator	Sapphire 1.998 mm	Sapphire 1.993 mm	Sapphire 1.869 mm	Sapphire 1.986 mm	Sapphire 1.992 mm	Sapphire 1.879 mm
Sample	none 385 K	(0.337 mm) (625 K)	(0.503 mm) (540 K)	none 390 K	(0.360 mm) (560 K)	(0.501 mm) (505 K)
Window	Sapphire 3.418 mm	LiF 3.069 mm	LiF 3.069 mm	Sapphire 3.413 mm	Sapphire 2.874 mm	Sapphire 3.054 mm
Peak Drive Pressure = 20 GPa Window coatings (sputtered): Al + TiN barrier + Ti adhesion + Ni (both substrates) Two-part molybdenum sample holder, extension brazed on						

Table 3-16: Z shot 1541

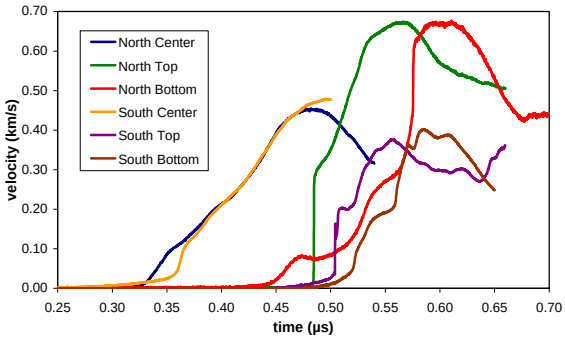

Figure 3-16: Z shot 1541

sign incorporated insulators between panels and an apparatus to passively transfer heat out of the panels. The high-temperature VISAR probes incorporated vent tubes, which appeared to significantly reduce the amount of buffer material deposited on the window. The pulse shape was modified to better mimic a shot in high-inductance mode at the foot of the pulse. Indium bonding was used at all insulator/panel interfaces, but several of these failed due to lack of a sufficient barrier layer on the copper panels. These were pressed and held in place by applying adhesive around the edge of the insulator, which appears to have worked at least some of the time (for example, North Center). Due to a miscommunication, the sapphire insulators were not thickness-matched within each panel. With the dual-sample heater body, this led to improper seating of the sample holders on the insulators, causing variations in liquid sample thickness and large scatter in temperature measurements. Two of the samples shown (North Bottom and South Bottom) were probably in a solid state during the shot. In addition, many of the velocity profiles have significant uncertainty due to a noise problem with one of the VISAR systems' source lasers.

If the issues that prevented this shot's goal from being reached are addressed, then there will be a good chance on the next shot of obtaining a complete set of data at known temperature and sample thickness with useful drive measurements. Most of these issues are straight-forward to address; insulators above and below the panel assembly for temperature uniformity, matched sapphire insulator thickness for accurate temperature and thickness, and improvements to the VISAR system already being undertaken. The indium bonds are the only issue possibly requiring further development. One approach to avoid bond problems altogether would be to continue development of the cup-insert design of Figure 2-5, which would also allow much higher overdriving pressures.

3.2. Preliminary Analyses

As detailed in the previous section, most of the experiments performed to date on liquid tin failed to produce velocity profiles that can be analyzed quantitatively for information on either the EOS or solidification kinetics. Preliminary analyses consist of attempts to reproduce the experimental velocity curves using one-dimensional finite-difference computations with a multi-phase continuum model for tin. This requires drive measurements that can be used to accurately predict a time-varying boundary condition for use in wave propagation calculations that include the sample. Only a few of the shots have provided such data, and these are considered here.

3.2.1. Three-Phase Continuum Model for Tin

The three-phase continuum model used here is based on three assumptions introduced by Horie and Duvall (1968) concerning a homogeneous mixture of different structural phases of a single material; (1) common particle velocity, (2) common pressure and temperature, and (3) no interfacial energy between phases. The calculation method follows that developed by Andrews (1971) and extended to *N* phases by Hayes (1975). Each of the pure phases (α-solid, γ-solid, and liquid) has its own EOS, and extensive properties of the mixture are mass-averaged over all phases. For the EOS of each phase, a Mie-Grüneisen form is assumed with constant c_v, constant Γ/v, and the reference $p(v)$ curve given by a Birch isotherm. EOS parameters and reference-state values for the three phases of tin are based on those given by Mabire and Héreil (2000). The phase boundaries in Figure 1-1 were computed by solving for states where the Gibbs free energies of two phases are equal.

Transformation kinetics is introduced by a simple phenomenological model wherein the rate of change of mass fraction for a given phase is proportional to the weighted sum of the differences in Gibbs free energy from each other phase;

$$\dot{x}_i = \sum_j \frac{G_j - G_i}{A_{ij}}, \tag{3-1}$$

where A_{ij} is a constant of proportionality (in units of energy × time) for transformation from phase *i* to phase *j*. In addition, a constant Gibbs energy offset ΔG_{ij} can be specified for each transformation to represent metastable and hysteretic behaviors; for a given loading rate, this implicitly defines a characteristic time having the effect of a nucleation time. The model was implemented in the one-dimensional wave propagation code WONDY [Kipp and Lawrence, 1982].

It is important to note that the above model, based solely on macroscopic thermodynamics, is not intended to illuminate the underlying physics of dynamic solidification. Rather, the goal is to connect experimental data to continuum modeling. Confidence in the the model was obtained by successful comparison [Hayes, 2000] to the impact data of Mabire and Héreil (2000), which encompass melting upon release from Hugoniot states in the γ-solid phase.

It was the intent of the LDRD project to replace Equation 3-1 with a more physically-based model informed by results from molecular-dynamics calculations. Due to time spent addressing problems with the experiments, this was never accomplished. Such a model might include separate time scales for nucleation (either homogeneous or heterogeneous) and growth of the solid phase [Shekar and Rajan, 2001], and possibly a third time scale for late-stage coalescence of solid grains [Rappaz *et al*, 2003]. It would also need to include the effects of over-pressurization rate on solidification [Luo *et al*, 2004]. The computational results for interface velocity and interface energy from Section 5.2 will be useful in the development of a model for kinetics of solidification in tin.

3.2.2. Backward-Forward Analysis Technique

The shape of the compression wave entering the liquid tin sample depends not only on the shape of the current pulse, but also on the complicated processes of magnetic-field diffusion and joule heating occurring in the thin power-flow layer of the anode. Assuming that the isentropic compression responses of the anode, insulator, and window materials are known, a time-resolved measurement of a material interface where there is no sample (*i.e.*, a drive measurement) can be used to calculate an effective loading profile by numerically integrating the one-dimensional equations of motion backward (upstream) in Lagrangian coordinate from the measurement position [Hayes, 2001]. The computed stress history at the upstream integration endpoint, when used as the boundary condition of a forward wave-propagation calculation that neglects magnetic field effects, reproduces the measured velocity profile. If the upstream computed stress history lies outside the causal region of influence of the interface where the drive measurement was taken, then it is also an effective loading history for a configuration where the window used for the original drive measurement has been replaced by another

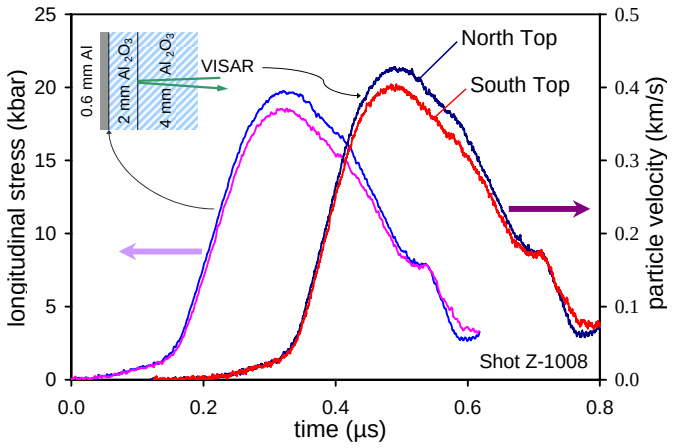

Figure 3-17: Example of drive measurements (red and dark blue curves) and backward integration results (magenta and light blue curves) from Z shot 1008.

material such as liquid tin, assuming the two locations were driven by the same magnetic pressure history. Thus the drive velocity measurement on one part of a panel provides an effective boundary condition for calculating propagation of the stress wave through the another part of the panel, without resorting to magneto-hydrodynamics.

A drive measurement example corresponding to Z shot 1008 is shown in Figure 3-17. Velocity measurements at the sapphire/sapphire interface were backward integrated to obtain the longitudinal stress histories at the aluminum/sapphire interface. At late time, the measured velocity profiles were corrected to account for motion of the back surface of the window, which affects the optical path length, under the assumption that sapphire compresses linearly. For the backward integrations, elastic sapphire is modeled as hydrodynamic (no strength) using the Mie-Grüneisen EOS referenced to the elastic Hugoniot of Barker and Hollenbach (1970), with Γ_0=1.5. Thermal softening of the sapphire elastic constants causes at most a 1% change in longitudinal modulus for the temperatures of interest [Tefft, 1966], and was therefore neglected. The drive measurements in Figure 3-17 were on two different anode panels and show slightly different peak stress; it is not known whether such differences arise from anode/cathode misalignment, thermal distortion of the panel assembly, or some combination of the two.

Some backward and forward calculations include pre-heated aluminum (on shots without insulators) or pre-heated LiF, for which thermal softening of the bulk modulus can be significant. The isentropic compression response in these cases was taken from Sesame EOS table 3700 for aluminum [Kerley, 1987] and table 7270 for LiF [Johnson, 1994].

3.2.3. Backward-Forward Results for Specific Shots

Backward-forward analysis as described in Sections 3.2.1-2 was performed using data from five of the experiments detailed in Section 3.1. Where possible, drive measurements were used from the same panel as the sample. Kinetically frozen calculations were done by setting $A_{liq\text{-}\gamma} = 10^6$ erg-s to ascertain the limiting case of no solidification, extrapolating the liquid tin EOS to higher pressure. Quasi-equilibrium calculations were done by setting $A_{liq\text{-}\gamma} = 10^{-4}$ erg-s. In some cases the sample thickness was varied by trial and error to obtain a reasonable match between experimental and computed arrival time. This always leads to sample thickness greater than that given in Section 3.1, and is justified by the difficulties in measuring liquid sample thickness (see Section 2.2.4).

Saturn Shot 2970

This one shot using a Pyroceram® insulator is considered here because it produced very different wave profiles than any other experiment. The anomalous compression response for the light-colored old batch of Pyroceram® was determined from a separate impact experiment, in which a symmetric tantalum impact drove a shock wave into a 3-mm thick sample. The measured wave speed *vs*. density curve was extrapolated to higher stress using a polynomial fit, which put the cross-over from anomalous to normal compressibility at about 10 GPa. The South panel drive measurement was backward integrated through the Pyroceram®, the result then used in forward calculations with quasi-equilibrium kinetics; see Figure 3-18. The thickness of both samples had to be increased significantly to match arrival time of the lower part of the waves (compare to thickness values in Table 3-4). The

computations show a plateau at the same velocity as the plateau in the measurements. In the calculation, this corresponds to solidification in the bulk of the liquid tin, away from the low-impedance LiF window. But the computations also indicate a much higher peak velocity than measured. While this may be due at least in part to an asymmetric load (the drive measurement was not taken on the same panel as the samples), it could indicate an unknown physical process. The difference between this experiment and others (which did not exhibit the behavior seen here) was determined to be sample purity; the samples on Saturn shot 2970 were contaminated by at least 2% aluminum (see Section 2.2.5), some of this probably in solid form.

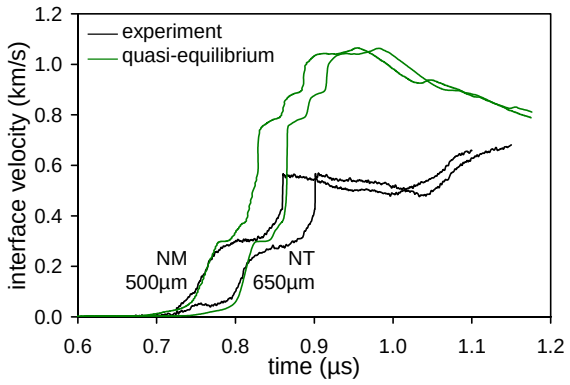

Figure 3-18: Comparison of measurements and quasi-equilibrium calculations for Saturn shot 2970.

Z Shot 964

This shot without insulators produced some clean-looking data, but it appears to have serious problems with sample thickness and drive measurements. As shown in Figure 3-19, the sample thickness had to be increased 35-60 μm (compare to Table 3-8), which is on the order of that due to bowing of the cup insert predicted by finite-element analyses of this configuration. The drive measurements were taken at LiF window interfaces located on each panel outside the insulated cup insert but on the vertical centerline. The calculations show consistently lower peak velocity than the experiment, suggesting a problem with either the vertical uniformity of power flow due to the insulated cup insert, or the EOS model for pre-heated LiF. Interestingly, only the middle-thickness sample (EB), which was also the highest-temperature sample, showed a plateau in velocity that may be related to solidification.

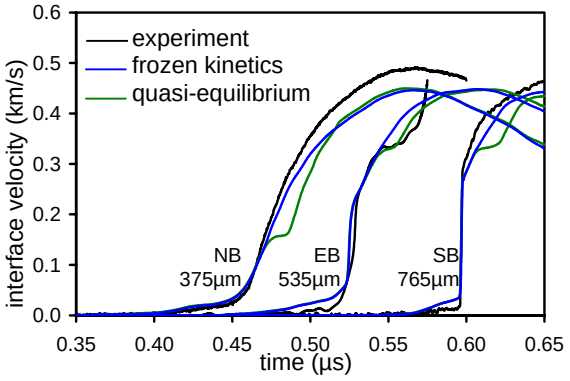

Figure 3-19: Comparison of measurements and quasi-equilibrium calculations for Z shot 964.

Z Shot 965

This experiment produced the first data that reasonably matched computed arrival times without modifying the measured sample thickness, as shown in Figure 3-20 (compare to Table 3-9). The curves for East Bottom (EB) have been shifted -50 ns for clarity. It also provided a comparison between sapphire and LiF windows at similar sample thickness. Due to problems with the drive measurements, the calculations relied on a boundary condition that was constructed from parts of both the East and West panel drive results. The experimental results are clearly represented more accurately by the frozen-kinetics calculations than by the quasi-equilibrium calculations, suggesting that the solidification process in tin is slow relative to the time scale of the experiment. It is not known

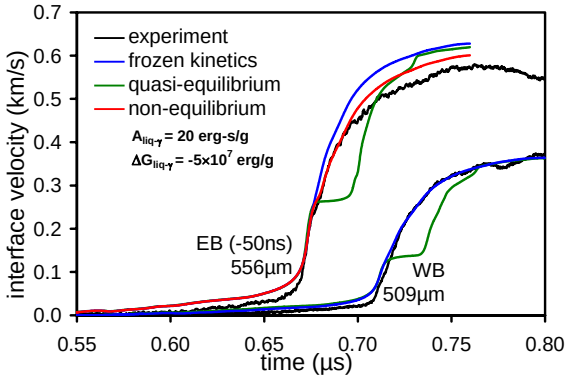

Figure 3-20: Comparison of measurements and quasi-equilibrium calculations for Z shot 965.

why the calculations overestimate the velocity during the initial foot of the wave, though the discrepancy may be within experimental uncertainty since the velocity corresponds to only about 10% of an interferometer fringe. In an attempt to more closely match the measured velocity profile for the EB sample, non-equilibrium calculations were performed using intermediate values for $A_{liq\text{-}\gamma}$ to slow the transformation, as well as non-zero $\Delta G_{liq\text{-}\gamma}$ to delay or promote the initial onset of the transformation. By adjusting the parameters to the values shown in Figure 3-20, it was possible to reproduce the initial departure from the frozen-kinetics velocity profile. The subsequent apparent decrease in wave speed, however, could not be captured using the present model.

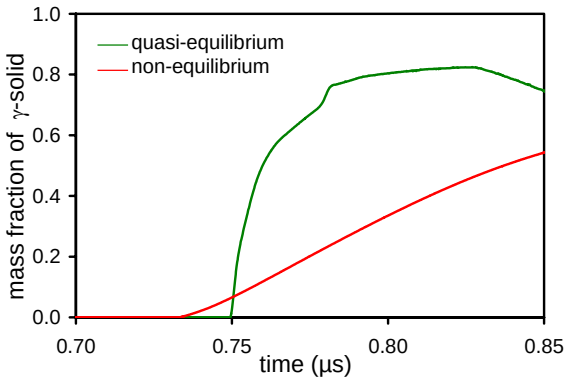

Figure 3-21: Comparison between quasi- and non-equilibrium computed mass fraction of γ-solid tin at the LiF window interface for Z shot 965 East Bottom.

The relatively minor difference between computed EB velocity curves in Figure 3-20 under quasi-equilibrium and non-equilibrium assumptions belies a significant difference in solidification as shown in Figure 3-21, which plots mass-fraction of solid γ-phase tin at the EB tin/LiF interface. Note that the tin does not fully transform at the LiF interface even under the equilibrium assumption, since the pressure remains low due to the mismatch in acoustic impedance between tin and LiF.

Z Shot 1007

Although it produced lower quality data, this shot is included here because it used a configuration identical to that of Z shots 965 and 1008. As shown in Figure 3-22, the calculations cannot match more than a small part of the measured velocity profile regardless of how much the sample thickness is increased (see Table 3-10 for measured thicknesses). The problem is most likely due to gaps having opened up in the glue bonds between the aluminum panels and sapphire insulators (see Section 2.2.9). Calculations to include such a gap have not been attempted. Like Z shots 965 and 1008, there is no evidence of a plateau in velocity that could indicate rapid solidification.

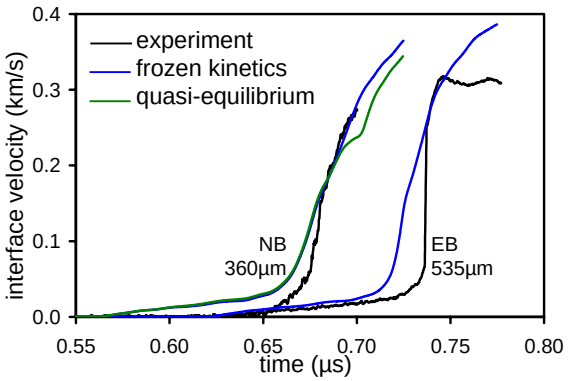

Figure 3-22: Comparison of measurements and quasi-equilibrium calculations for Z shot 1007.

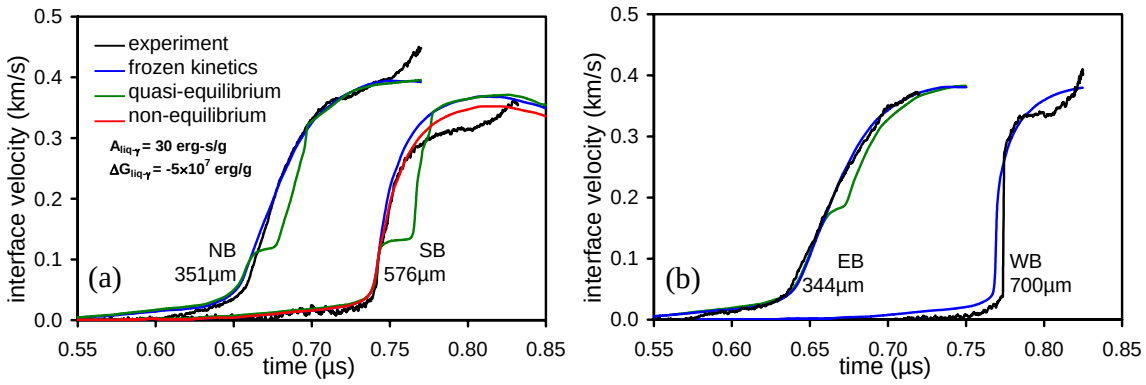

Figure 3-23: Comparison of measurements and quasi-equilibrium calculations for Z shot 1008.

Z Shot 1008

All four samples on this shot produced data. These are compared to calculations in Figure 3-23. To match computed arrival times, sample thickness had to be increased for South Bottom (SB) and West Bottom (WB), the latter by an unusually large amount (about 25%; see Table 3-11). As for Z shot 965, frozen-kinetics calculations better reproduce the experimental results than quasi-equilibrium calculations. For the SB sample, a non-equilibrium calculation using the parameter values shown in Figure 3-23a (which are slightly different from those used for Z shot 965 EB) could reproduce the initial departure of experiment from the frozen-kinetics calculation, but not the subsequent apparent decrease in wave speed. Three of the samples show a velocity increase at late time that is not captured by calculations. This cannot be attributed to known wave interactions because the wave velocity is very low in liquid tin; one can only speculate that the behavior might be related to solidification occurring somewhere inside the tin sample. In Figure 3-24 is plotted the mass-fraction of solid γ-phase tin at the tin/sapphire interface for the SB sample.

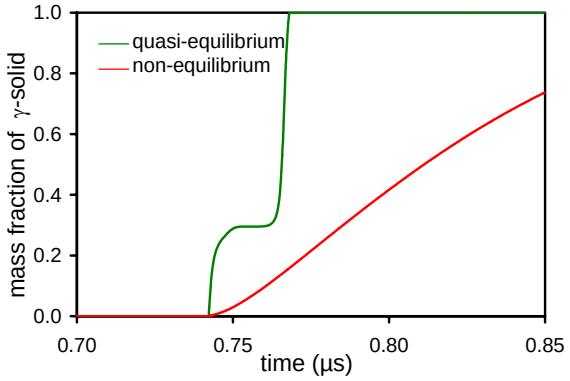

Figure 3-24: Comparison between quasi- and non-equilibrium computed mass fraction of γ-solid tin at the sapphire window interface for Z shot 1008 South Bottom.

3.2.4. Backward Minimization Technique and Results

The tentative conclusion drawn above from backward-forward analyses, that solidification may occur in dynamic experiments but is slow relative to the duration of the present experiments, can be investigated using a second, different analysis technique of backward minimization. The technique is shown schematically in Figure 3-25. The velocity measurement at the sample is backward integrated along with the drive measurement to a common position outside the sample's region of causal influence (here taken as the panel/insulator interface). The difference between the two computed stress histories is minimized by allowing the parameters describing the response of the liquid tin to vary during iterative backward integrations of the sample's velocity history. The calculations explicitly assume that the propagating wave is a simple wave (where wave speed is equal to sound speed and is single-valued in longitudinal stress), and that the materials' behaviors are well described by single-valued compression isentropes without time-dependent effects. Further details of this technique have been described elsewhere [Hayes, 2001; Davis, 2005].

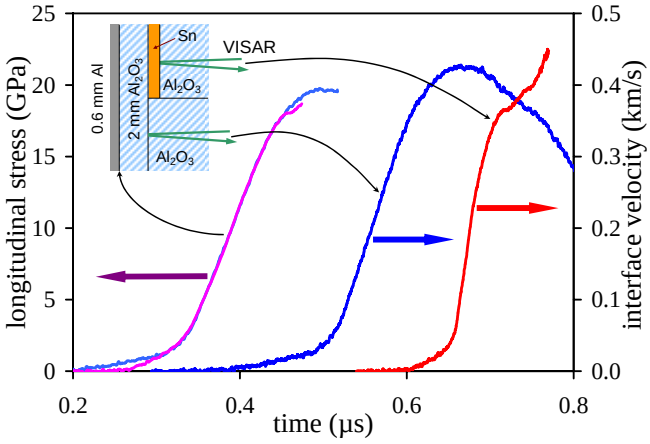

Figure 3-25: Example of backward minimization technique; inputs are NT (blue) and NB (red) velocity measurements from Z shot 1008, and outputs are parameters of Sn EOS that minimize differences between longitudinal stress histories (light blue and magenta).

The measurements for Z shots 965 and 1008 (except WB) were fit in this manner by using an isentrope for liquid tin expressed in terms of Lagrangian sound speed c_L as a fourth-order polynomial in pressure. For the two thin samples (Z-1008 EB and WB), the minimization pro-

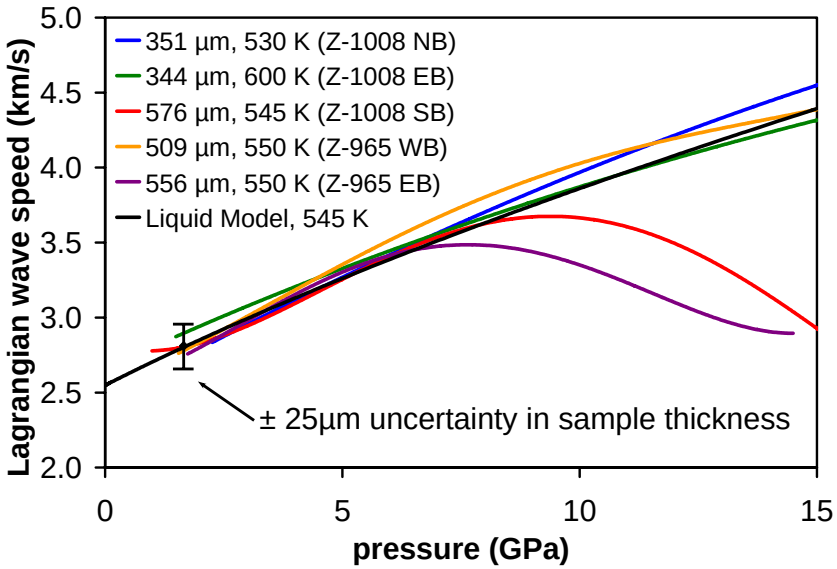

Figure 3-26: Backward-minimization results for five liquid tin samples on Z shots 965 and 1008; two of the thick samples show clear departure from the thin samples and from the liquid model at high pressure.

cedure converged on a close match between effective stress histories over a wide range in stress, as shown in Figure 3-25. The three thicker samples did not converge as well, due probably to the method's sensitivity to initial conditions, but also suggesting that the chosen c_L–p polynomial is not an accurate representation of the tin's behavior in those cases. To obtain a better fit, these minimizations were instead performed in three stages; first fitting a polynomial only over the lower half of the wave, then using a second polynomial to fit the upper half of the wave (with the parameters for the lower-pressure polynomial fixed at their previously-found values), and finally fitting a single polynomial over the full stress range using an initial guess found by fitting a single polynomial to the previous two-segment result. Sample thicknesses were taken from Figures 3-20 and 3-23, and include the increased thickness for Z-1008 SB (576 µm instead of 554 µm from Table 3-11) based on backward-forward analysis.

The c_L–p curves thus obtained are presented in Figure 3-26 along with a curve computed from the liquid-tin model (extrapolated to higher pressure where the equilibrium phase is γ-solid). The two samples that could not be matched by frozen-kinetics calculations in Section 3.2.3 (Z-965 EB and Z-1008 SB) show a significantly lower apparent wave speed than the other samples or the model above 10 GPa. The discrepancy is larger than the possible error due to uncertainty in sample thickness, which itself was quite large for these experiments. One interpretation for this is that the lower apparent wave speed is consistent with the non-equilibrium calculations in Section3.2.3. Another interpretation is that the large discrepancy between thick and thin samples on the same shot (Z-1008) indicates a violation of the rate-independence assumption behind the backward minimization technique. The result is consistent with a time dependent response above 10 GPa due to a slowly initiating solidification transformation. It is not clear why Z-965 WB does not behave like the other samples of similar nominal thickness.

The above evidence for solidification is far from conclusive, and further experiments are needed with accurately known sample thickness, and preferably samples of two or more thicknesses at the same initial temperature. The five later shots described in Section 3.1 did not reach these goals due to numerous technical issues described earlier.

4. COMPUTATIONAL APPROACH

The goal of the computational part of this investigation was to obtain information about the structure and equation of state (EOS) of liquid tin (Sn) at high pressure and to obtain information about the kinetics of the solidification process during dynamic compression. Molecular dynamics (MD) simulations were used to address these properties. Molecular dynamics simulations require a prescription for the potential energy and interatomic forces as a function of the atomic coordinates. In this study, two different prescriptions were used. In the study of the structure and EOS of the molten state, the forces were obtained from *ab initio* calculations using density-functional theory (DFT). These calculations determine the forces from a density-functional treatment of the quantum-mechanical description of the electrons. While highly predictive and accurate, the density-functional MD simulations are very computationally intensive. Therefore, it is not feasible to use this approach for the study of dynamic processes such as solidification. Instead, simulations based on empirical potentials were used to study the kinetic aspects. A new empirical potential for the simulation of Sn was developed. This potential was optimized to match the prediction of the forces in the density-functional simulations. The empirical-potential MD simulations were used to determine the interfacial velocity as a function of temperature and pressure, and also to explore the limits of supercooling/over-pressurization of the liquid state.

4.1. Density-Functional Molecular Dynamics

This section describes the *ab initio* molecular dynamics study of the properties of molten Sn as a function of temperature and pressure. There are various motivations for this study. The first is that knowledge of the EOS of the liquid will benefit the experimental dynamic compression experiments. The second motivation is that Sn is an interesting material to study due to the potential for unusual behavior. There are experimental indications of non-simple behavior of the liquid in the form of the observed static structure factor, $S(q)$. At low temperatures, a small shoulder is observed on the high-q side of the first peak in $S(q)$. This shoulder disappears at higher temperatures. It is speculated to result from residual tetrahedral bonding in the molten state. It is of interest to know how this shoulder evolves as a function of pressure in addition to temperature. Sn is also an interesting material in terms of the nature of its bonding and structure. The interatomic interactions are intermediate between forms favoring close-packed and open structures. This can be seen in two ways. The elements above Sn in the periodic table, C, Si, and Ge, are all diamond-structure semiconductor crystals at ambient conditions. The element below Sn, Pb, is a close-packed fcc metal under ambient conditions. Sn itself is stable in the diamond structure at low temperature and pressure, but at higher temperatures and/or high pressures, it is stable in more densely packed metallic structures. This structural polymorphism in the solid state suggests that there may be interesting variations in the short-range order in the liquid state.

The structural polymorphism of Sn also suggests that it is important to perform *ab initio* based simulations. The effective interatomic interactions may well be substantially dependent on density and local environment. The present simulations determine the energies and forces from a density-functional treatment of the quantum mechanics of the electrons. This will capture any environmental dependence of the interactions. Simulations based on interatomic potentials may not be able to cover a wide range of densities and temperatures. An alternative approach to the one in the present work is to develop effective interatomic potentials for each density and temperature under consideration. Bernard and Maillet (2002) have recently applied this approach to Fe and Sn.

The energy calculations are based on density functional theory calculations of the electronic structure. This is a well-established technique for computing the energy and structure of materials [Kaxiras, 2003; Martin, 2004]. The calculations are performed in the local density approximation (LDA) to the exchange and correlation energies. The electron-ion interaction is treated by a norm-

conserving pseudopotential that was developed by Wright (2003) using the approach of Hamann (1989). The pseudopotential treats the 5s and 5p electrons. The 4d electrons are treated as part of the ionic core. Since the 4d states are close in energy to the 5s and 5p states, it is not clear that they can be treated via the ionic pseudopotential. Preliminary calculations were performed with a pseudopotential that did not include the 4d electrons in the ionic core, but rather treated them explicitly. Comparison of results from the two pseudopotentials indicated that it was not necessary to treat the 4d electrons explicitly. The calculations were performed using a plane-wave basis set with a cutoff energy of 16 Ryd. For the solid phase calculations, the k-space integrations were performed using the Monkhorst-Pack scheme. For the liquid state calculations, the energy and forces are based on the gamma point. The calculations were performed using the SOCORRO code developed at Sandia National Laboratories.

The structure and thermodynamics of the liquid state were computed *via* completely *ab initio* molecular dynamics. The forces for a given atomic configuration are computed from the density-functional theory calculations. The equations of motion of the atoms are computed from these forces using the Verlet algorithm [Frenkel and Smit, 1996]. Temperature control is obtained using the stochastic algorithm of Anderson (1980). The simulations used a time step of about 5 fs and ran for about 1000 time steps or 5 ps. The average internal potential energy and the pair correlation function are computed by a standard time average over the simulation. The static structure factor, $S(q)$, is computed for wave vectors that correspond to the reciprocal lattice of the simulation cell. These values are also time averaged and then binned according to the magnitude of q to obtain the spherically symmetric result.

An important quantity of interest is the pressure. It is possible to compute the stress tensor, and so the pressure, directly for each configuration in the MD simulation. This would be the most direct route to computing the pressure. However, there are two numerical limitations to this approach. First, the calculation of the stress tensor in an electronic structure calculation converges more slowly as a function of the number of k points than does the calculation of the energy. Thus a higher k point sampling would be required to compute the pressure and that dramatically increases the computational requirements. The second issue is that the instantaneous pressure in an MD simulation fluctuates strongly in time during an MD simulation. Thus long time averages would be required in order to obtain reliable values of the pressure.

In order to avoid these issues, an alternative approach was used here to determine the pressure. For a given temperature, simulations were performed at a variety of volumes. This is not really extra work since the long-range goal is to study the properties as a function of pressure, or alternatively, density. From these simulations, the volume derivative of the internal potential energy can be obtained. The pressure, though, is related to the volume derivative of the free energy. Thus the entropy must be known. The entropy is estimated from an equivalent hard sphere liquid. In order to determine the packing fraction of the equivalent hard sphere liquid, the hard sphere diameter is adjusted to fit the Percus-Yevick solution for the static structure factor to the static structure factor computed directly in the simulation [Theile, 1963; Wertheim, 1963]. Once the hard sphere diameter is known, the entropy and pressure of the equivalent hard sphere liquid can be computed from the Percus-Yevick hard-sphere EOS [Hansen and McDonald, 1986]. This is combined with the pressure derivative of the potential energy to obtain the pressure of the liquid.

4.2. Empirical-Potential Molecular Dynamics

The potential used to describe Sn is a combination of an embedded atom method (EAM) form and a Tersoff potential form. The EAM form is well established as appropriate for metals in the absence of significant covalent bonding [Daw *et al*, 1993]. The Tersoff form has been used to describe systems, such as Si, where covalent bonding of the sp electrons leads to tetrahedral bonding geometries [Tersoff, 1988]. The energy as a function of the atomic coordinate will therefore be written as

$$E = \sum_i E_i\left(\sum_{j\neq i} e_j\left(r_{ij}\right)\right) + \frac{1}{2}\sum_{ij,i\neq j}\varphi_{ij}\left(r_{ij}\right) + \frac{1}{2}\sum_{ij,i\neq j} V_{ij}^{tersoff}\,. \tag{4-1}$$

The first two terms are the standard EAM terms and the last term is for the Tersoff potential. It should be noted that $V^{tersoff}$ depends on the local environment so this does not represent a simple pair interaction as will be discussed below.

The simple EAM pair potential is taken as a modified Morse potential,

$$\varphi(r) = E_M\left(\frac{1}{\varepsilon-1}e^{-a_M(r-r_0)} - \frac{\varepsilon}{\varepsilon-1}e^{-\varepsilon a_M(r-r_0)}\right). \tag{4-2}$$

In the standard Morse form, $\varepsilon = 2$. The current form was chosen to give more flexibility to the pair potential form while maintaining the interpretation of r_0 as the location of the potential minimum and E_M as the depth of the potential. The EAM density term is taken here to have the form

$$e\left(r\right) = e_{0,1}r^{n_1}e^{-a_1 r} + e_{0,2}r^{n_2}e^{-a_2 r}\,. \tag{4-3}$$

This form is modified at short distances. For each term, the maximum value of this density function occurs at $r = (n/a)$. For distances $r < (n/a)$, the maximum value is used instead of the actual form. This avoids unphysical small values of the density function at short distances. For both the pair potential and the density, the functions are cut off by simply subtracting the value of the function at the cut-off distance.

The embedding function is determined numerically by requiring that the total energy as a function of lattice constant for the body-centered cubic (BCC) structure be reproduced. The BCC phase was chosen in this case because it is convenient, the energy *vs*. lattice constant function could be determined by first-principles calculations, and it is close to the body-centered tetragonal (BCT) structure that is relevant to the pressures of interest. The energy *vs*. volume is parameterized using the Rose EOS given by

$$E(a) = -E_{sub}(1 + a^* + 0.35a^{*3})\exp(-a^*)\,, \tag{4-4}$$

where a^* is the scaled lattice parameter

$$a^* = \frac{1}{s}\left(\frac{a}{a_0} - 1\right), \tag{4-5}$$

and s is the scaling parameter

$$s = \sqrt{\frac{E_{sub}}{9B\Omega}}\,. \tag{4-6}$$

Here B is the bulk modulus and Ω is the volume per atom.

The Tersoff potential uses the same functional forms as the parameterizations that have been developed for Si [Tersoff, 1988]. In particular, the potential is given by

$$V_{ij}(r_{ij}) = f_C(r_{ij})\left[f_R(r_{ij}) + b_{ij}\,f_A(r_{ij})\right], \tag{4-7}$$

where the repulsive and attractive parts of the interactions are given by the simple exponentials

$$f_R(r) = A\exp(-\lambda_1 r) \text{ and} \tag{4-8}$$

$$f_A(r) = -B\exp(-\lambda_2 r)\,. \tag{4-9}$$

The functional form used for the cutoff function, $f_{C,}$ is

$$f_C(r) = \begin{cases} 1, & r < R - D \\ \frac{1}{2} - \frac{1}{2}\sin\left[\frac{\pi}{2}(r-R)/D\right], & R - D < r < R + D \\ 0, & r > r + D \end{cases} \quad (4\text{-}10)$$

The term b_{ij} contains the dependence of the strength of the attractive portion of the potential on the local bonding environment of atoms *i* and *j*. This is the source of the local environment dependence of the potentials as well as the angular dependence of the interactions. It is defined through the following series of equations:

$$b_{ij} = \left(1 + \beta^n \zeta^n\right)^{-1/2n}, \quad (4\text{-}11)$$

$$\zeta_{ij} = \sum_{k \neq i,j} f_C(r_{ik}) g(\theta_{ijk}) \exp\left[\lambda_3^3 (r_{ij} - r_{ik})^3\right], \text{ and} \quad (4\text{-}12)$$

$$g(\theta) = 1 + \frac{c^2}{d^2} - \frac{c^2}{d^2 + (h - \cos\theta)^2}. \quad (4\text{-}13)$$

In these equations, the subscripts *i*, *j* and *k* refer to atoms, r_{ij} is the distance between atoms *i* and *j*, and θ_{ijk} is the angle between the bonds *ij* and *ik*. The remaining constants are parameters of the potential.

The various parameters in this potential were adjusted to fit a large database of first-principles information about the energetics of Sn. This included the zero-temperature energy-volume relations for a variety of crystal structures including face-centered cubic (FCC), BCC, BCT, A4 (grey Sn), A5 (white Sn), A15 and simple cubic. The elastic constants of the BCC phase were also fit. In part, this ensured that the BCT phase is stable relative to the BCC phase at the relevant pressures by enforcing the mechanical instability of the BCC lattice to a tetragonal distortion. Finally, force matching was used for a liquid state configuration near the melt line. In this case, the forces on the individual atoms computed with the potential model are compared with the forces obtained from DFT calculations on the same atomic configuration. This provides input into the detailed forces that lead to the liquid structure.

Due to the large number of parameters as well as the large number of quantities used in the fit, the process of finding an optimal parameter set was quite challenging. In this work, the DAKOTA (Design Analysis Kit for Optimization and Terascale Applications) software package from Sandia National Laboratories was employed [Eldred *et al*, 2003]. In particular, genetic algorithms were used to determine a reasonable set of parameters. The resulting parameter set was then used as the starting point for a local optimization of the parameters. The use of the

Parameter	Value	Parameter	Value
r_0	3.15697 Å	E_{sub}	4.13 eV
E_M	0.27045 eV	a_0	3.77 Å
a_M	1.28961 Å^{-1}	s	0.2002
ε	2.29606	n	20
$R_{cut,\,Morse}$	6.31395 Å	β	1.84593
n_1	0.939613	c	2.04415
a_1	1.38716 Å^{-1}	d	1.08448
$e_{0,1}$	20.0985	h	-0.33333
n_2	1.17908	λ_1=λ_2	1.21191 Å^{-1}
a_2	1.81192 Å^{-1}	λ_3	17.1405 Å^{-1}
$e_{0,2}$	15.2572	R	3.7 Å
$R_{cut,density}$	4.84735 Å	D	0.5 Å

Table 4-1: The parameters defining the empirical potential for Sn as described in the text.

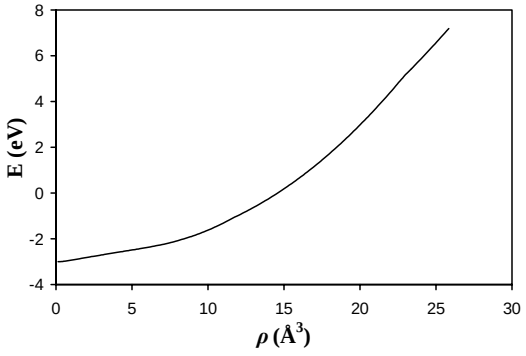

Figure 3-1: The embedding function used for the empirical potential of Sn as described in the text.

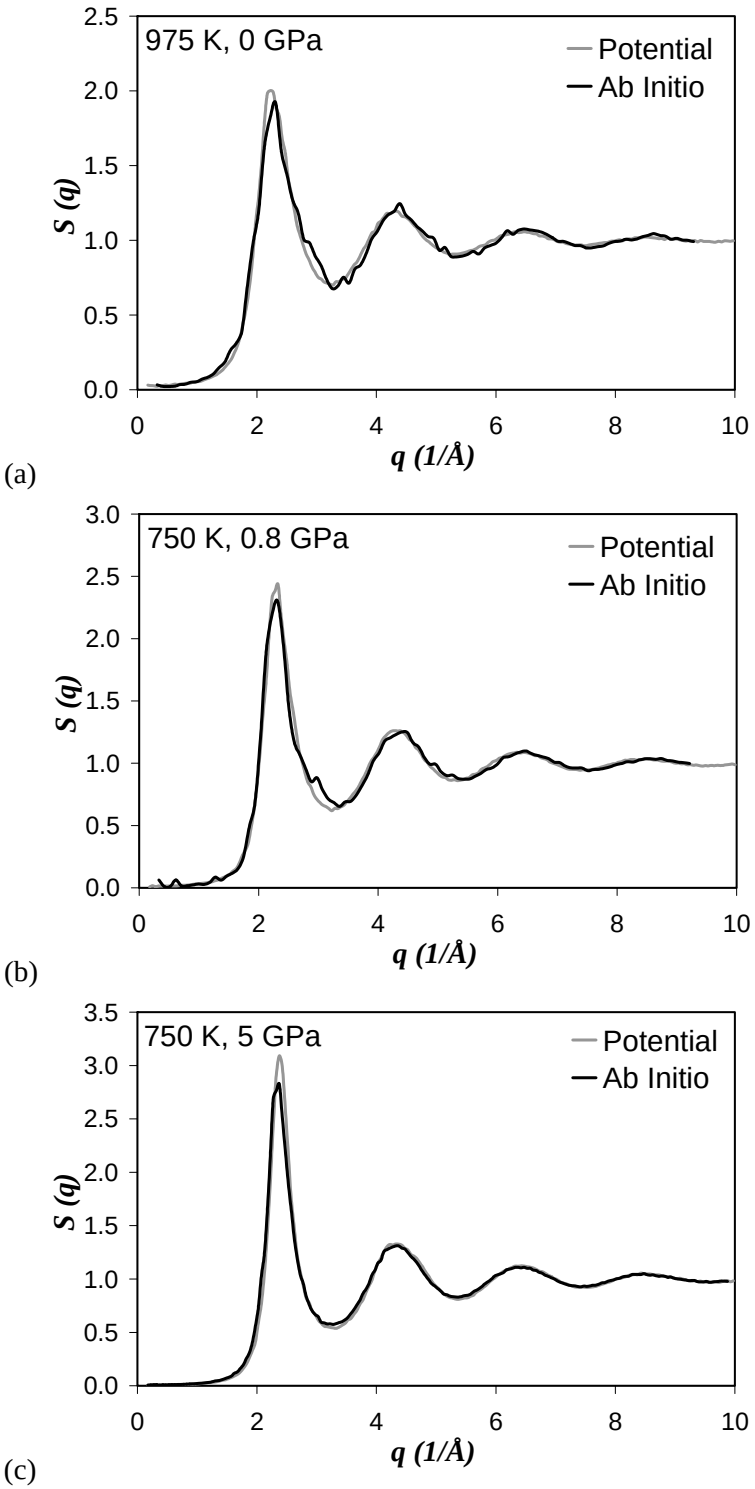

Figure 4-2: Comparisons of the static structure factor of molten Sn computed with density functional MD (black curves) and with empirical-potential MD (grey curves) for (a) 975 K and 0 GPa, (b) 750 K and 0.8 GPa, and (c) 750 K and 5 GPa.

DAKOTA optimization toolset dramatically reduced the effort required to optimize the parameter set. The parameters thus determined are presented in Table 4-1. The embedding function is displayed in Figure 4-1.

It is important that the interatomic potential provide a realistic description of the interactions in the liquid state. That is the reason for fitting to the forces for a prototypical liquid snapshot. In order to test the ability of the resulting potentials to describe the liquid state, the structure factor determined by the *ab initio* density-functional theory calculations were compared with the structure computed using the interatomic potential model. In both cases, the structure factor, $S(q)$, is computed from molecular dynamics simulations. The densities for the simulations were based on the DFT pressure predictions for the given temperature and pressures and were the same for both the DFT calculations and the empirical-potential calculations. The temperatures and pressures compared were 975 K and 0 GPa, 750 K and 0.8 GPa, and 750 K and 5.0 GPa, as shown in Figure 4-2. Note that there is significantly greater noise in the DFT results due to the smaller system size, 256 atoms, and shorter simulation times for these calculations. Overall, the agreement between the empirical-potential calculations and DFT calculations is very good. The consistent point of disagreement is that there appears to be a small shoulder on the high-q side of the first maximum in $S(q)$ in the DFT results which is not present in the empirical potential results.

5. COMPUTATIONAL RESULTS

The computational results fall into two broad areas; the determination of the properties of molten Sn under high pressures, and the determination of the kinetics of solidification. The determination of properties is based on density-functional MD calculations presented in Section 4.1. Some of the results presented in this section are for either zero temperature or zero pressure. Such calculations have been performed in order to provide validation of the computations against known properties of Sn under these conditions. Additional calculations address the properties of the melt at conditions of interest. The calculations of the kinetics of solidification, described in Section 5.2, are based on the empirical potentials described in Section 4.2. These calculations include the determination of the solid-liquid interfacial velocity as a function of temperature and pressure. In addition, the limits of supercooling/over-pressurization for the case of homogeneous nucleation of the solid phase are addressed.

5.1. Density-Functional MD results

5.1.1. Equilibrium Crystal Structure

In order to validate the pseudopotential used in the density-functional calculations, the energy-volume relationships of a variety of possible crystal structures were computed for zero temperature. The stable phases predicted by the calculations were then compared with the known phase diagram. The experimental temperature-pressure phase diagram of elemental Sn [Liu and Bassett, 1986] is presented in Figure 5-1. Note that there are a variety of stable solid crystal structures. Since the calculations here are for zero-temperature, the relevant phases are those that occur at low temperatures. At low pressure, the equilibrium structure is diamond cubic (A4). This is the "gray tin" phase. It has an open atomic structure with tetrahedral coordination. The next stable phase with increasing pressure is the metallic "white tin" phase. This phase is denoted A5 and is formed from two interpenetrating body-centered tetragonal lattices. This phase also appears at zero pressure for temperatures above 13°C, indicating that the energy difference between the gray tin and white tin structures should be small. With increasing pressure, another metallic phase with a simple body centered tetragonal (BCT) structure becomes stable. Finally, at very high pressures, the tetragonal distortion of the BCT phase is lifted and the BCC phase becomes stable.

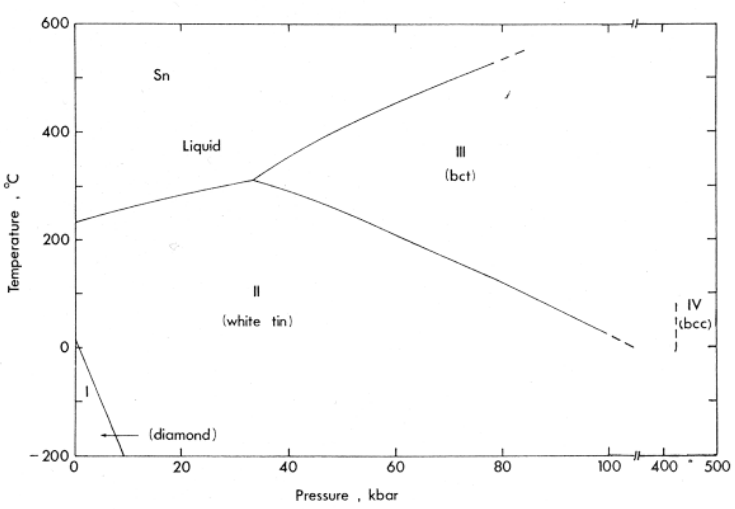

Figure 5-1: Experimental pressure-temperature phase diagram of Sn [Liu and Bassett, 1986] (1 kbar = 0.1 GPa).

In Figure 5-2, the computed energy-volume curves are plotted for a variety of simple crystal structures. In addition to the experimentally observed stable phases, the simple cubic (SC) and the A15 crystal structure were considered. Calculations were also performed for the face-centered cubic (FCC) and body-centered cubic (BCC) crystal structures, but for readability, these results are not included in the Figure 5-2. The FCC structure is never found to be the stable phase. The BCC phase

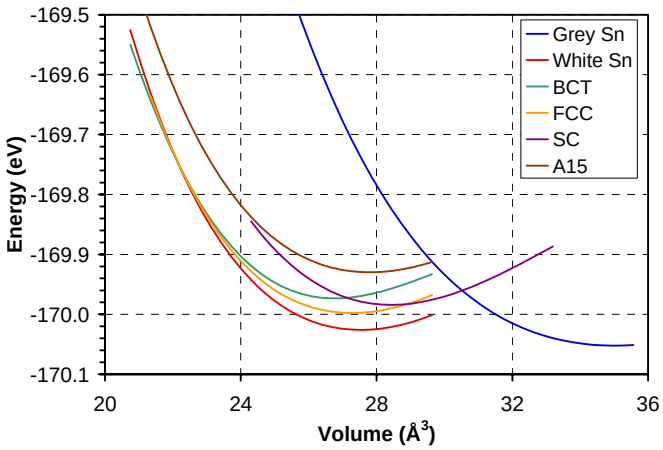

Figure 5-2: Energy-volume curves for a variety of phases of Sn computed by density-functional theory.

results appear to cross the BCT results for high densities. Since this occurs at pressures much higher than of interest in the present work, the details of the crossing were not evaluated. For the white tin and BCT structures, the energy plotted is the minimum with respect to the *c/a* ratio for that fixed volume. In the case of white tin, the *c/a* ratio was found to be 0.54 over the range of volumes considered This is in agreement with the experimentally observed ratio. For the BCT structure, the *c/a* ratio is a function of the volume with the ratio increasing for decreasing volume (increasing pressure).

The computed energy-volume curves are in good accord with the experimental phase diagram. The lowest energy structures present are the experimentally observed stable structures. The A15 and SC cubic structures are higher in energy, consistent with the absence of these phases in experiment. The transition pressures at zero temperature can be determined from the Maxwell common-tangent construction. The transition from the gray Sn structure to the white Sn structure is computed to occur at 1 GPa. This is in good agreement with the phase diagram in Figure 5-1. The transition from white Sn to the BCT structure occurs at 14 GPa. This is consistent with experiment; the transition occurs at 10 GPa at room temperature, with a transition pressure that increases with decreasing temperature. The *c/a* ratio in the BCT phase is computed to be 0.89 at the transition. This is somewhat smaller than the experimental values that range from 0.91 at 10 GPa and room temperature to 0.94 at 50 GPa. This small discrepancy may be due to errors in the DFT energy. The computed minimum with respect to *c/a* is very broad for the BCT phase so minor errors in the energy could lead to this discrepancy. Note also that the experimental values are for finite temperature (room temperature) while the calculations are for zero temperature. It is possible that finite-temperature effects may change the equilibrium value of *c/a*. The results presented here are also consistent with previous computational studies of the phase stability of Sn [Cheong and Chang, 1991; Corkill *et al*, 1991; Christensen, 1993a; Christensen and Methfessel, 1993b].

Another test of the solid-state calculations is to compare predicted and measured equilibrium lattice constants of the two zero-pressure phases. Since the calculations were performed at zero temperature, the experimental lattice constants were adjusted to zero temperature based on the thermal expansion of that phase. (Note: this does neglect the contribution of zero-point motion of the ions to the lattice constant.) For gray Sn, the experimental lattice constant is 6.482 Å. The calculations give 6.54 Å. For the white Sn phase, the experimental lattice constants are a = 5.8123 Å and c = 3.1577 Å. The calculated lattice constants are a = 5.89 Å and c = 3.18 Å. Note that the experimental and calculated values of *c/a* are both 0.54. Overall, the computed lattice constants are approximately 1% higher than the experimental values.

5.1.2. Thermal Expansion

A simple, yet important, property of a molten metal is its density as a function of temperature. The ability to predict this quantity provides a good test of the ability to predict the EOS of the melt. The calculations were actually performed for a set of volumes at a given temperature. The results of the calculations were then fit to simple polynomials to allow interpolation to zero pressure. The relative density (ρ/ρ_{melt} at zero pressure) as a function of temperature is plotted in Figure 5-3 along with two sets of experimental results [Nasch and Steinemann, 1995; Alchagirov and Chocheava, 2000]. While the relative densities show good agreement with experiment, the absolute calculated densities

are consistently lower than the experimental values. This is similar to, though of greater magnitude than, the larger lattice constants predicted by density-functional calculations compared with experiment. This reflects the approximations inherent in the pseudopotential and local density approximation treatment of the electronic structure. This accounts for about half of the discrepancy in the predicted density. The other half must result from the approximate treatment of the liquid entropy. It is encouraging to note that the thermal expansion of the liquid is predicted quite accurately. This indicates that relative densities predicted from the calculations should be quite accurate. The better agreement for the relative densities is not surprising since the contributions to the errors in the density would be expected to cancel when looking at relative densities.

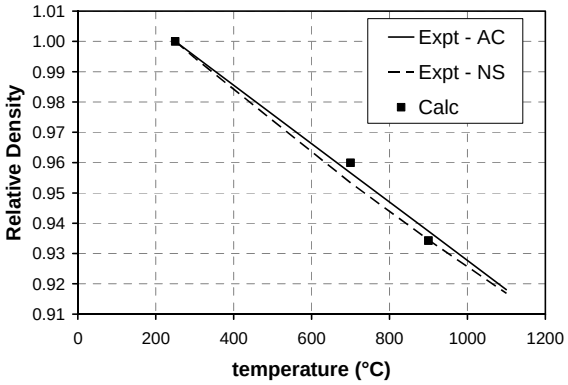

Figure 5-3: The density of the liquid phase relative to its density at the melting point. The squares are computed values and the curves are experimental results from Nasch & Steinemann (1995) (dashed) and from Alchagirov & Chocheava (2000) (solid).

5.1.3. Static Structure Factor

The nature of the short-range order in the molten state as a function of temperature and pressure is of interest in general and for Sn in particular. The most common experimental measure of the local ordering in a liquid is the static structure factor, $S(q)$, which can be measured by X-ray or neutron diffraction. There have been many experimental determinations of the structure factor for Sn near the melting point [Gamertsfelder, 1941; North *et al*, 1968; Waseda and Suzuki, 1972; Vahvaselkä, 1978; Waseda, 1980; Zou *et al*, 1987]. In Figure 5-4, the computed structure factor is compared with that obtained by Waseda. The data of Waseda were chosen because they are presented in a tabular fashion that facilitates the comparison. The overall agreement between the calculations and the experiment is excellent and is similar to the level of agreement between the various experimental determinations. In particular, the position and amplitudes of the maximums and minimums are reproduced. Note that there is a small shoulder on the high-q side of the first maximum in the $S(q)$. This has been observed in all of the experimental observations performed near the melting point. This is of interest since it indicates a deviation of the local ordering from that obtained in simple hard sphere models. It is believed to be a reflection of tetrahedral ordering in the liquid. This shoulder is also present in the calculated structure factor, which indicates that the density-functional calculations correctly reproduce this subtle feature.

There exist few experimental studies of the variation of the static structure factor with temperature and pressure. In Figure 5-5, the computed static structure factor for densities corresponding to zero pressure is presented for 525 K, 975 K, and 1175 K. With increasing temperature, the amplitude of the oscillations in $S(q)$ decrease. This trend is the expected behavior of the liquid structure with increasing temperature. It is important to note that the shoulder on the first peak of $S(q)$ is observed near the melting point but not in the results at higher temperature. Waseda (1980) has tabulated experimental results for the static structure factor at these temperatures; these data are also presented in Figure 5-5. Note that the trends are the same as

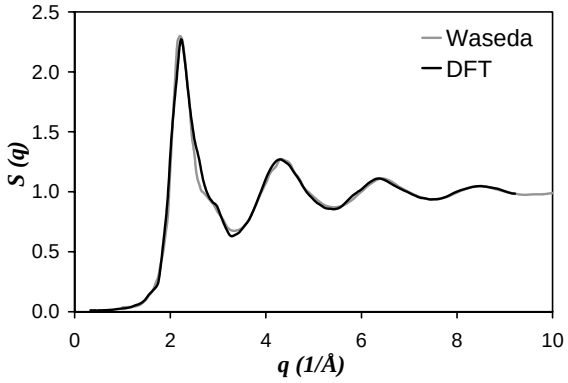

Figure 5-4: The static structure factor of molten Sn at 525 K and 0 GPa; present computational result (black) and experimental result of Waseda (grey).

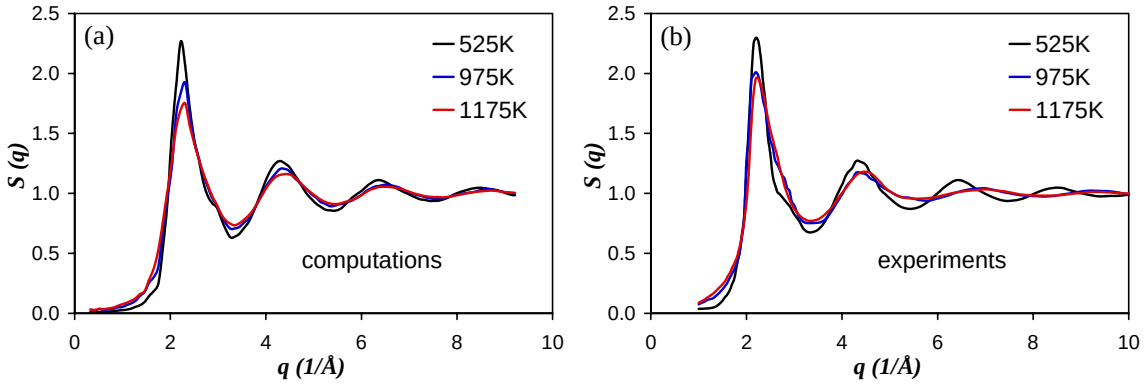

Figure 5-5: The static structure factor of molten Sn at 0 GPa and 525 K, 975 K, and 1175 K, (a) as computed by density-functional theory based MD, and (b) from the experimental results of Waseda (1980).

those observed for the calculated data. The quantitative agreement, though, between the computed and experimental structure factors at the higher temperatures is not as good as that obtained near the melting point. In particular, the amplitude of the first peak changes more substantially between 975 K and 1175 K for the computational results than for the experimental results. The similarity of the first peak for the experimental results is somewhat surprising and may point to issues with the experiments. It is important to note that the shoulder on the first peak is also absent in the higher temperature experimental results, in accord with the current calculations.

The static structure factor was computed for a variety of temperatures and pressures, the latter in the range of 0–7 GPa. The results for 750 K and 975 K are presented in Figure 5-6. The variation with pressure is consistent with general expectations. In particular, at higher pressures and thus higher density, the first peak of the structure factor increases. This is consistent with simple hard sphere pictures of the liquid structure where the amplitude of the first peak is largely determined by the effective packing fraction of the liquid. The remaining oscillations of the structure factor are only weakly affected by the changes in density. There was initial speculation of a liquid–liquid phase transformation in Sn based on some preliminary isentropic compression experimental results (see Section 3.1). In a liquid–liquid phase transformation, there are two different liquid phases with differing local structures. The current results do not support the existence of such a phase transformation. If such a phase transformation where present, it would be expected that there would be more significant changes in the static structure factor than are observed in the present calculations. Since the computed variation of structure with pressure is consistent with the variation expected based on

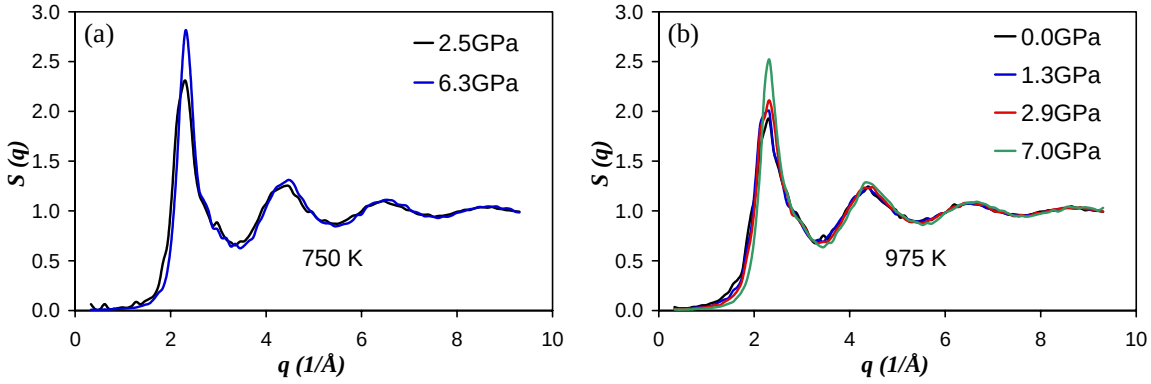

Figure 5-6: Computed structure factors at (a) 750 K for densities of 0.0377 $Å^{-3}$ and 0.0347 $Å^{-3}$, which correspond to computed pressures of 6.3 GPa and 2.5 GPa respectively, and (b) at 975 K for densities of 0.0377 $Å^{-3}$, 0.0347 $Å^{-3}$, 0.0333 $Å^{-3}$, and 0.0320 $Å^{-3}$, which correspond to computed pressures of 7.0 GPa, 2.9 GPa, 1.3 GPa, and 0 GPa respectively.

simple hard-sphere models, there is no reason to believe that a liquid–liquid transition occurs in the present temperature and pressure range. (Simulations were also performed at 1175 K, but those results are not presented since the variations are similar to those in Figure 5-6.) It should be pointed out that simulation times for the density-functional MD are quite short, on the order of 5 ps. It is possible that the simulations do not have time to find the true equilibrium structure. Therefore, the absence of evidence for a liquid–liquid transition can not be taken as conclusive.

5.1.4. Specific Heat

One of the key thermodynamic quantities for the continuum description of the dynamic compression of molten tin is the specific heat. The constant-volume specific heat is the temperature derivative of the internal energy evaluated at constant volume. The density-functional molecular-dynamics simulations were used to provide a computational evaluation of the specific heat. The internal energy of molten Sn can be broken into three components; the kinetic energy of the ions, the potential energy associated with the ionic configurations, and the thermal excitation of the electronic energy. Each component is discussed below. The specific heat is evaluated on a per atom basis, then converted to engineering units.

Temperature determines the kinetic energy of the ions explicitly in the classical limit. The energy associated with ionic kinetic energy is $(3/2)k_BT$, and the contribution to specific heat is $(3/2)k_B$.

The *ab initio* calculations determine the average potential energy of the system. This calculation assumes that the electronic system is in its ground state, the Born-Oppenheimer Approximation. One can evaluate the constant-volume specific heat by examining the potential energy for various temperatures at a constant volume. The computed values are presented in Figure 5-7 for two different volumes. In both cases, the potential energy is seen to vary linearly with temperature with approximately the same slope for both of the volumes shown. On a per-atom basis, this slope gives a contribution of $1.16k_B$ to the specific heat. Note that this value is somewhat less than the Dulong-Petit value of $(3/2)k_B$. The fact that they differ is not surprising since the Dulong-Petit value is based on the assumption of a harmonic solid and the system considered here is a liquid.

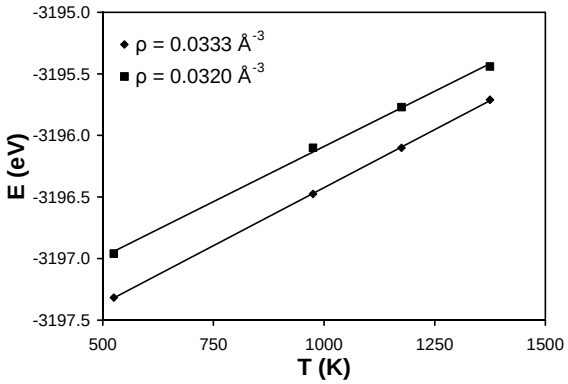

Figure 5-7: The potential energy of a 256 atom cell as a function of temperature as computed by density function MD.

The final contribution to the specific heat is the excitation of electron states near the Fermi level. The specific heat associated with this can be directly related to the density of electronic states at the Fermi level [Ashcroft and Mermin, 1976]. The expression is

$$c_v = \frac{\pi^2}{3} k_B^2 T g(\varepsilon_F), \qquad (5\text{-}1)$$

where $g(\varepsilon_F)$ is the density of electronic states at the Fermi level. This quantity can be obtained from the *ab initio* molecular-dynamics simulations, which determine the electron energy levels at each time step. These can be examined to obtain the electronic density of states. In particular, the simulations were performed at a single k-point. To obtain the density of states, a Gaussian broadening of each computed energy level is used to determine the overall density. The density of states for configurations at 525 K and 975 K, both at a density of $\rho = 0.0333$ Å^{-3} is plotted in Figure 5-8.

The cut-off of the density of states around 0.4 is an artifact of the calculations. The simulations only calculate the lowest energy levels and this cut-off reflects the restricted number of energy levels

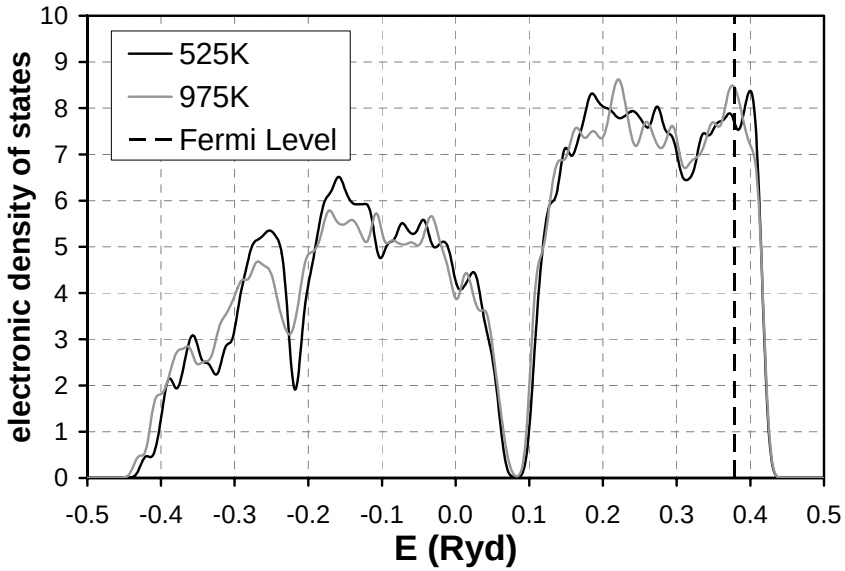

Figure 5-8: The electronic density of states computed from density-functional MD at 525 K and 975 K. The energy is given in Rydbergs. Note that the roll off of the density of states around 0.4 Ryd. is an artifact of the calculations.

that are actually computed. The energies in Figure 5-8 are given in Rydbergs and the density of states is normalized to states per atom. An interesting feature of the computed density of states is the dip just below 0.1 Ryd. The total number of electrons in the region below the dip corresponds to the s states. The upper portion of the density of states is therefore dominated by the p states.

Using the value for 525 K in Equation (5-1) for the electronic specific heat yields 0.09 k_B. The above results are in units of k_B per atom. The conversion factor to engineering units is

$$\frac{k_B}{\text{atom}} = \left(\frac{8.315x10^3}{M} \right) \frac{\text{J}}{\text{kg} \cdot \text{K}} = 70.05 \frac{\text{J}}{\text{kg} \cdot \text{K}}, \tag{5-2}$$

where M is the atomic mass in amu and the last expression is specific to Sn (M = 118.69 amu). Combining the above contributions gives the following values for the constant-volume specific heat of molten Sn based on the *ab initio* molecular-dynamics simulations:

$$C_v = 2.75 \frac{k_B}{\text{atom}} = 193 \frac{\text{J}}{\text{kg} \cdot \text{K}} \text{ at 525 K (just above melting point), and} \tag{5-3}$$

$$C_v = 2.82 \frac{k_B}{\text{atom}} = 198 \frac{\text{J}}{\text{kg} \cdot \text{K}} \text{ at 1000 K.} \tag{5-4}$$

5.2. Empirical-Potential MD Results

One of the quantities required for the evaluation of solidification rates is the velocity of a planar solidification front as a function of temperature and pressure. The interfacial velocities were computed using the empirical interatomic potential described in Section 4.2. The behavior of the interfacial velocity as a function of both pressure and temperature was used to evaluate how the velocity relates to the net thermodynamic driving force. In the dynamic solidification experiments, the system is expected to encounter the solid-liquid coexistence line in the region where the liquid is in equilibrium with the body-centered tetragonal (BCT) phase. Thus, the interface velocity was evaluated for an interface between the BCT and liquid phases. The basic idea is to create an initial state that contains

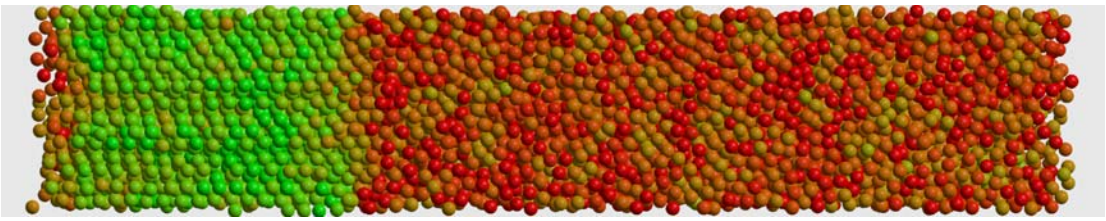

Figure 5-9: Snapshot of a typical initial state for the empirical-potential molecular-dynamics simulations. The green atoms have local atomic arrangements close to the BCT structure while the red and orange atoms have liquid local environments.

both solid and liquid phases. Simulations are then performed at a variety of temperatures and pressures, and the motion of the interface is determined. While the basic outline of the calculations is straightforward, there are various simulation details that need to be handled correctly.

The simulations were performed in a rectangular cell with periodic boundary conditions in all three directions. An example of an initial simulation cell is shown in Figure 5-9, where the coloring of the individual atoms reflects the degree to which the local atomic arrangement conforms to the solid BCT phase. The green atoms are solid while the red and orange atoms are in the liquid phase. The solid crystal is oriented such that the [001] direction is normal to the interface, *i.e.*, along the long direction of the cell. In this orientation, the shorter c direction of the BCT structure is normal to the interface.

The simulations were performed in a constant-temperature, constant-pressure ensemble. The temperature thermostat used was simple velocity rescaling. Every ten time steps, the velocities of all the atoms are rescaled so that the kinetic energy of the system corresponded to the desired temperature. The pressure was maintained *via* a restricted version of the Paranello-Rahman (PR) method [Frenkel and Smit, 1996]. In the full PR approach, the three periodic vectors of the cell are treated as dynamic variables. The motion of these periodic vectors is driven by the difference between the current strain in the system and the desired strain state. The current strain is computed using the standard virial expressions. Treating all three periodic vectors as dynamic variables, however, is not appropriate for the simulations being performed here. The solid-liquid interfaces have an interfacial stress associated with them. If all the periodic vectors are allowed to be variable, the system will evolve such that the total stress in the plane of the interface is zero. This total stress will contain a contribution from the two solid-liquid interfaces as well as from the bulk solid and liquid phases. In the computational cell, the ratio of interface to bulk is large and so the interfacial stress will have a strong influence on the interfacial area. In the physical system, the bulk regions will be much larger and the bulk stresses will dominate. In order to simulate those conditions, the cross-sectional area of the cell in the plane of the interface is held constant. The value of the periodic repeat length in the transverse directions is determined by the lattice constant *a* of the BCT phase at the desired temperature and pressure. The overall pressure in the system is maintained by adjusting the length of the cell in the manner of the PR method. As the system solidifies or melts, therefore, there is a slow change in the length of the cell in order to compensate for the volume change on melting and to maintain the desired overall pressure.

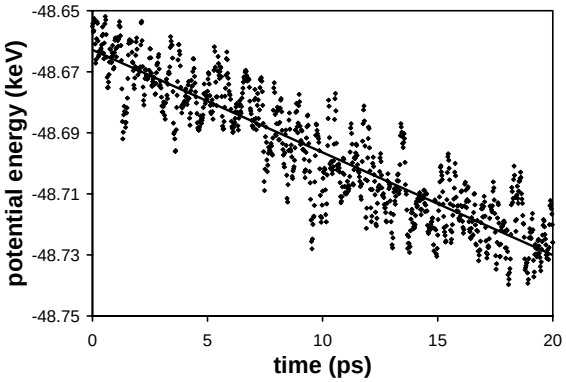

Figure 5-10: The time dependence of the potential energy in a MD simulation of a domain containing a solid-liquid interface (see Figure 5-9) for a temperature of 750 K and pressure of 10 GPa. The solid line is a linear fit to the data.

The interface velocity was determined by examining the time evolution of the potential energy, *U*, of the system. Due to the latent heat associated

with the transformation, the average potential energy will either decrease or increase with time, depending on whether the system is solidifying or melting, respectively. Superimposed on this average trend are the short-term fluctuations of the potential energy inherent in MD simulations. A typical example of the time dependence of the potential energy is shown in Figure 5-10. The points are instantaneous values of the potential energy at 0.02-ps intervals, and the solid line is a least-squares fit. The slope of the fit yields the average rate of change of the potential energy. The interfacial velocity is related to the change in potential energy by

$$v = \frac{dU/dt}{2A(u_s - u_l)}, \qquad (5\text{-}5)$$

where u_s and u_l are the potential energy densities (potential energy per unit volume) of the solid and liquid phases. The factor of two reflects the presence of two solid-liquid interfaces in the cell.

In order to implement the above procedure, the potential energy and equilibrium density of the solid and liquid phases need to be known as functions of temperature and pressure. In addition, the values of the solid BCT phase lattice constants, as a function of temperature and pressure, are required in order to set up the initial simulation cell. Therefore, molecular-dynamics simulations were

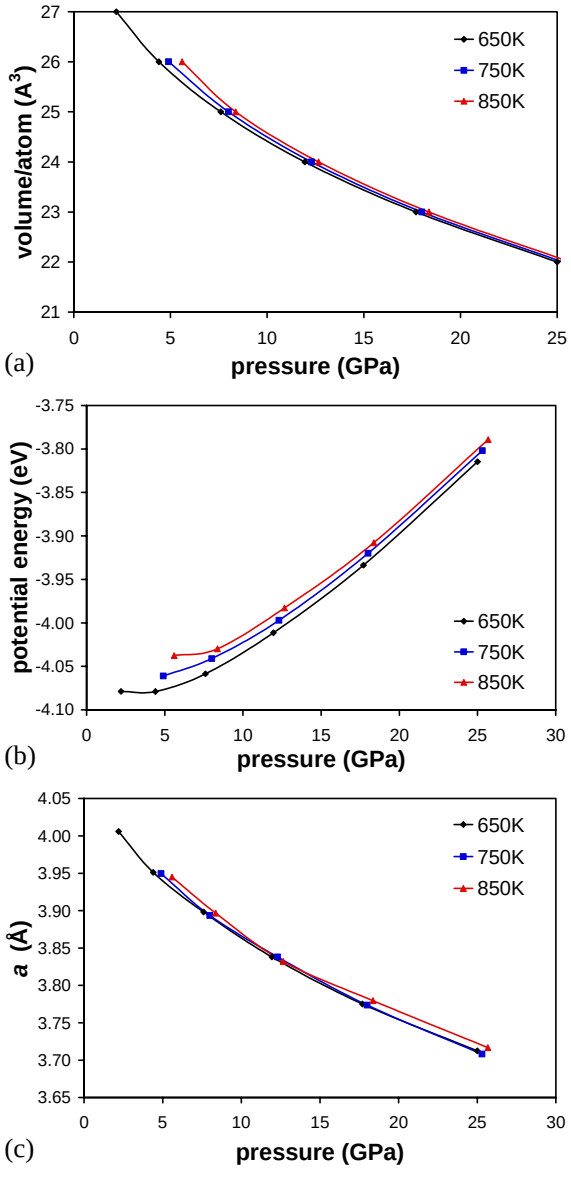

Figure 5-11: Computed (a) pressure, (b) potential energy, and (c) lattice constant *a* of the BCT solid phase from empirical-potential MD as a function of pressure for three different temperatures. The lattice constant *c* can be deduced from these results.

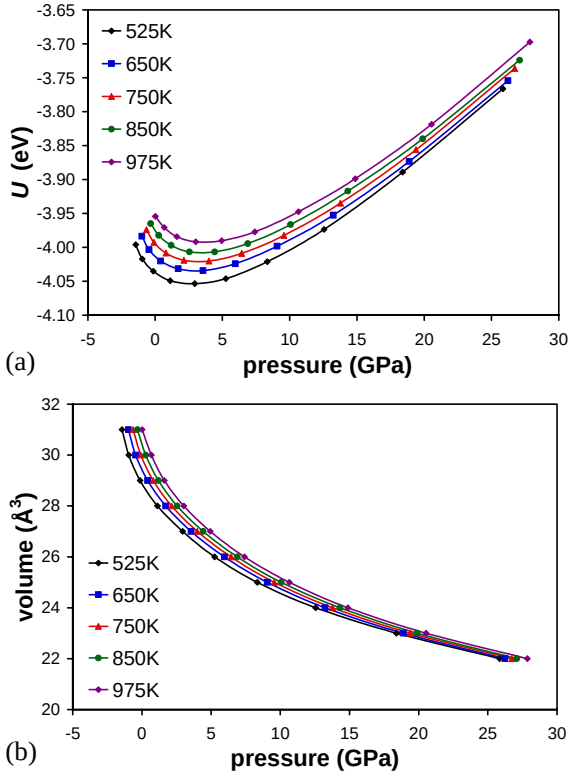

Figure 5-12: Computed (a) potential energy per atom and (b) volume per atom of the liquid phase from empirical-potential MD as a function of pressure for five different temperatures.

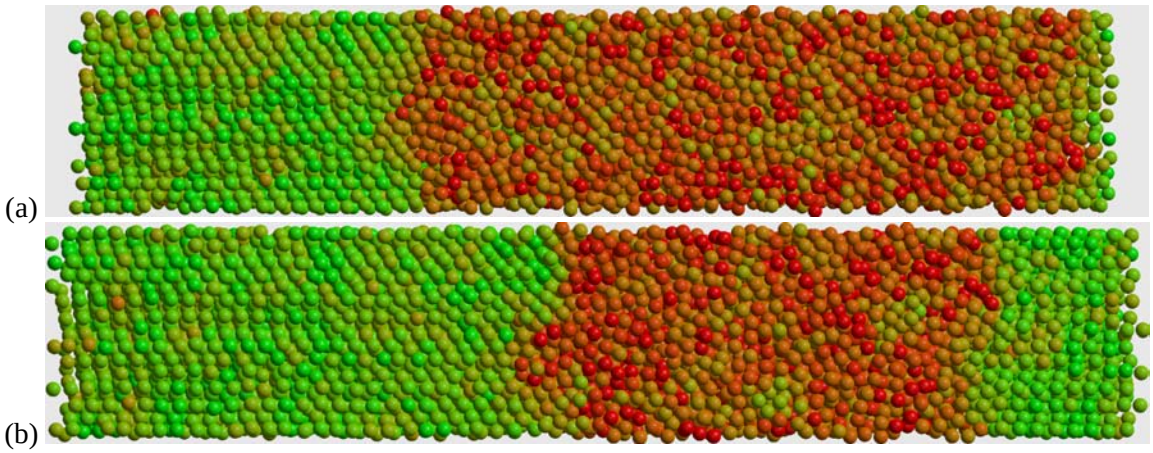

Figure 5-13: Two snapshots of the MD simulation of advancing solidification fronts for 750 K and 7.5 GPa. The snapshots are separated in time by 50 ps. The green shaded atoms have local atomic arrangements close to the BCT structure while the red atoms have liquid local environments.

performed for both the solid and liquid phases to determine the potential energy per atom, the volume per atom and the *a* and *c* lattice constants for the BCT phase. These simulations were performed at constant volume. For the solid phase, the simulations were performed for various values of *c/a*. The results were interpolated to determine the optimum *c/a*. The results of these calculations are shown in Figure 5-11. Simulations of the potential energy and pressure in the liquid state have also been performed. These simulations were performed at constant temperature and volume, and the results were interpolated to obtain the desired values. The potential energy and volume per atom as a function of pressure for the liquid state is shown in Figure 5-12.

An alternative approach to the determination of the interface velocity is to identify each atom as either solid or liquid, determine the location of the interface, and monitor its average position as a function of time. A convenient method of quantifying the degree to which a given atom is solid or liquid is to compare the positions of its neighboring atoms with the relative positions in an ideal BCT solid and compute the magnitude of the difference. Two snapshots of a MD simulation at 750 K and 7.5 GPa are shown in Figure 5-13. The shading reflects the magnitude of the difference in neighbor positions between the simulation and an ideal BCT lattice. The green atoms are solid and the red/orange atoms are liquid. Note that the solid-liquid interface has significant fluctuations and so is not clearly planar. As a result, there is significant ambiguity in the definition of a boundary plane location. This makes the direct approach to the determination of the interface velocity problematic. Some comparisons with the potential energy approach were made. The results were similar, though there was substantially more variation of the computed velocities when they were based on the direct determination of interface position. Thus the potential energy method was used for all subsequent analysis.

The interface velocity is presented in Figure 5-14 as a function of pressure for temperatures of 650 K, 750 K, and 850 K. Also shown are linear fits to the data for each individual temperature. The pressure where the interface velocity for a given temperature crosses zero gives the value of the equilibrium melting pressure at that temperature. These results therefore yield three points on the melt curve between the liquid phase and the BCT

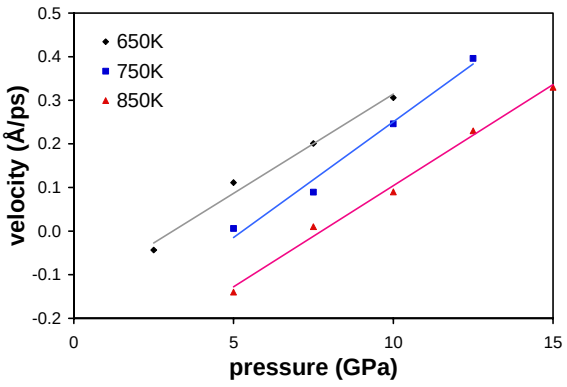

Figure 5-14: The computed interface velocity of a (001) solid-liquid interface as a function of pressure for temperatures of 650 K, 750 K, and 850 K.

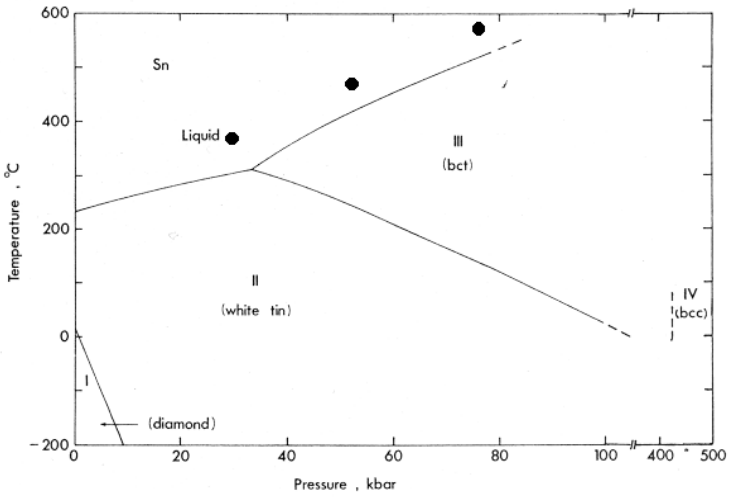

Figure 5-15: The experimental phase diagram of Sn [Liu and Bassett, 1986] with the three computed points on the melt curve shown as solid circles (1 kbar = 0.1 GPa).

solid phase. These points are placed on the experimental phase diagram in Figure 5-15. Note that the slope of the melt curve is in very good agreement with the experimental slope. The computed melt curve lies approximately 50 K above the experimental curve. This level of agreement on a computed melting point is quite reasonable for MD simulations.

The above results for the interface velocity can be reduced to a single curve. The interface velocity is expected to vary linearly with the difference in Gibb's free energy between the solid and liquid phases since this represents the thermodynamic driving force acting on the interface. Let us choose a point on the melting curve, (P_m, T_m). In the vicinity of that point, the free energy of each phase $i = l$ or s is given to first order by

$$G_i(P,T) \approx G_i(P_m,T_m) + V_{i,m}(P-P_m) - S_{i,m}(T-T_m)\,. \tag{5-6}$$

Note that the Gibb's free energy of the two phases are equal at (P_m, T_m), so we can write the free energy difference between the phases in this vicinity to first order as

$$\Delta G_{sl} = G_l - G_s \approx \Delta V_m(P-P_m) - \Delta S_m(T-T_m)\,. \tag{5-7}$$

The entropy difference at the melting point, ΔS_m, is related to the latent heat of the transformation. In terms of quantities that can be readily extracted from the molecular-dynamics simulations, the entropy difference is given by

$$\Delta S_m = \frac{\Delta H_m}{T_m} = \frac{\Delta U_m + P_m \Delta V_m}{T_m}\,. \tag{5-8}$$

A convenient point on the calculated melting curve for these results is (P_m, T_m) = (5 GPa, 740 K). Molecular-dynamics simulations were performed for both the solid and liquid phases at these conditions. From these simulations, it was found that ΔU_m = 0.046 eV/atom and ΔV_m = 0.60 Å^3/atom. From these results, one determines that $\Delta V_m = 3.6\times10^{-7}$ m^3/mole and ΔS_m = 8.5 J/(mole-K). The interfacial velocities are plotted versus the free energy difference in Figure 5-16. Within the statistical variation of the data, the results lie on a line with a slope of 0.013 (m-mole)/(J-s).

An important quantity is the maximum under-cooling and/or over-pressurization that can occur for the liquid state for a given heating or strain rate. This maximum is the point at which solidification would occur in the absence of any heterogeneous nucleation of the solid phase. Classical nucleation theory indicates that the formation of the solid phase proceeds by the creation of a nucleus of solid phase in the liquid. The energy to form such a nucleus depends on the free energy difference

between the solid and liquid phases as well as the interfacial free energy between the solid and liquid. Recently, Luo and co-workers have studied the systematics of superheating and super-cooling based on the ideas of classical nucleation theory [Luo and Ahrens, 2003a; Luo *et al*, 2003b]. They have also extended these ideas to the case of over-pressurization and de-pressurization. Their simulations of model Lennard-Jones systems indicate that there is a relationship between the maximum superheating (de-pressurization) and maximum super-cooling (over-pressurization) [Luo *et al*, 2004]. This approach will be followed here to estimate the maximum super-cooling (over-pressurization) based on a direct molecular dynamics simulation of the maximum superheating using the empirical potential. The maximum super-cooling and super-heating are related in classical nucleation theory since they both are determined by the same set of thermodynamic quantities – the solid-liquid interfacial energy and the free energy differences between the phases.

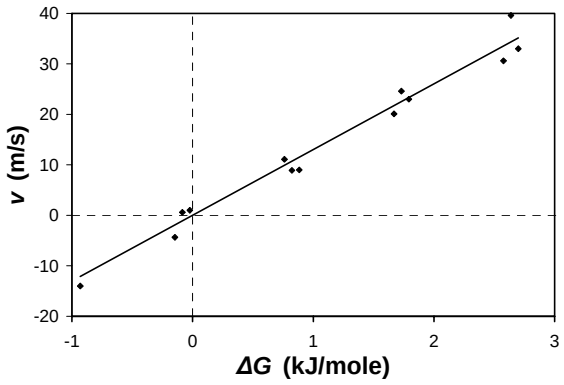

Figure 5-16: The interfacial velocity of a (001) solid-liquid interface in Sn as a function of the free energy difference between the solid and liquid phases.

In classical nucleation theory, there is a critical nucleus size where the free energy of formation of the nucleus is a maximum. Clusters larger than that size will grow and those smaller will shrink. The free energy required to form the critical sized spherical nucleus is given by

$$\Delta G_c(P,T) = \frac{16\pi\gamma_{sl}^3}{3(\Delta G_{sl} - E_\varepsilon)^2}. \qquad (5\text{-}9)$$

In this expression, γ_{sl} is the solid-liquid interface energy, ΔG_{sl} is the free energy difference per unit volume of the solid and liquid phases, and E_ε is the strain energy which will be neglected. The rate of nucleation will then be given by the rate at which critical sized nuclei form. This is given by

$$I = I_0 \exp\left(-\frac{\Delta G_c}{k_B T}\right) = I_0 \exp\left(-\frac{\beta}{\theta(\theta-1)^2}\right), \qquad (5\text{-}10)$$

where $\theta = T/T_m$ is reduced temperature, and the dimensionless quantity β is given by the expression

$$\beta = \frac{16\pi\gamma_{sl}^3}{3(\Delta H_m)^2 k_B T_m}. \qquad (5\text{-}11)$$

A main result of the work of Luo and coworkers is that the critical value of the exponent such that homogeneous nucleation will occur depends on the heating/cooling rate, Q. From the analysis of a variety of data, they develop the following form:

$$\frac{\beta}{\theta_c(\theta_c-1)^2} = A(Q) = 59.4 - 2.33\log_{10} Q. \qquad (5\text{-}12)$$

In this result, θ_c is the reduced temperature where the transition occurs.

The value of β for a given system can easily be determined from molecular-dynamics simulations. Isobaric simulations were performed with a thermostat where the temperature of the thermostat varies in time. This provides a constant heating rate. If the system is starting in the solid phase below the melting point, it can be heated until the system melts. Monitoring the macroscopic properties of the system such as its overall potential energy or volume can readily identify when the system melts.

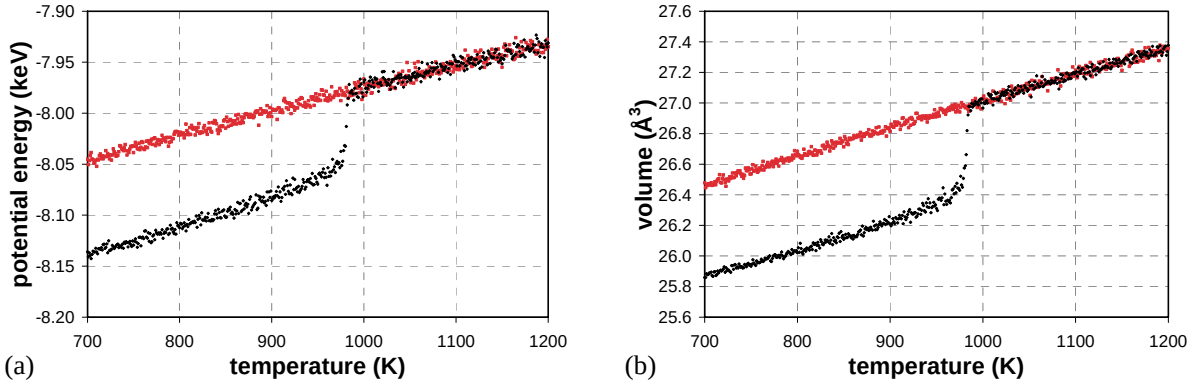

Figure 5-17: (a) potential energy per atom and (b) volume per atom as a function of temperature for a heating rate of 10^{12} K/s. The black squares are for simulations started from a liquid configuration, and the red diamonds are for simulations started from a solid BCT configuration.

The results of such a simulation are shown in Figure 5-17, which plots the volume and potential energy per atom as a function of temperature. The heating rate for these simulations is Q = 1 K/ps = 10^{12} K/s. Two simulations were run at a pressure of 5 GPa. In one the initial state was liquid. This provides the temperature-dependent values of the potential energy and volume. The other simulation started with a solid atomic configuration. In this case, the system was observed to melt at a temperature of 975 K. From the results above on the interface velocity, the melting point is known to be (P_m, T_m) = (5 GPa, 740 K). Thus the critical reduced temperature is θ_c = 1.32.

Given the value of θ_c, Equation (5-12) can be used to determine the value of β = 4.25. This value is smaller than the value of β = 5.4 deduced for Sn at zero pressure. This difference is to be expected since the low-pressure transition is between the liquid state and the white tin structure. The current result is for the transition between the liquid phase and the BCT phase. While Luo and coworkers argue that β should only be weakly pressure dependent, this argument is not expected to apply when the nature of the solid phase changes. The results in Figure 5-17 can also be used to determine the value of ΔH_m, the difference in enthalpy per unit volume between the liquid and solid BCT phases. The result for 5 GPa and 740 K is $\Delta H_m = 8.3\times10^8$ J/m^3. When this value is inserted into Equation (5-11), the average interfacial free energy between the solid and liquid phases at these conditions is estimated to be γ_{sl} = 120 mJ/m^2.

6. SUMMARY

6.1. Experimental Study

Prior to the LDRD project, some initial experiments had been performed on liquid tin at the Saturn and Z Accelerators. These data suggested the possibility of a liquid–liquid structural transformation, an important factor in the original LDRD proposal, as well as a rapid transformation of some kind (possibly solidification). Later experiments with higher-purity samples at the start of the project showed no evidence of a liquid–liquid transition, and limited evidence in some cases of a slow transition consistent with the onset of solidification. The latter evidence came from two different methods of analyzing measured velocity histories. The backward-forward method attempted to reproduce the measurements using an effective boundary condition obtained from backward integration of a drive measurement, a wave-propagation code with a multi-phase continuum model for tin, and a simple kinetics model (rate proportional to free-energy difference) allowing frozen-kinetics, quasi-equilibrium, or non-equilibrium assumptions for the solidification transformation. The data were generally best matched by the frozen-kinetics assumption, but much better agreement was found for two of the samples by using non-equilibrium kinetics with particular values for the rate proportionality constant consistent with a solidification time scale on the order of 100 ns. The backward minimization method determined for each sample a compression curve, in the form of a fourth-order polynomial in wave speed *vs.* pressure, that was most consistent with the corresponding drive measurement. The thin samples produced results within experimental uncertainty of the model for liquid tin (extrapolated beyond the equilibrium solidification curve). Two of the thick samples (in fact, the two requiring non-equilibrium kinetics in the first method) showed significant deviation at pressures above 10 GPa, consistent with lowered overall wave speed and/or the presence of time-dependent effects in that region.

Subsequent experiments attempted to reproduce these results with more accurately known sample thickness, but this goal was not attained due to numerous technical issues with the experiment design and the infrequent nature of experiments on the Z Accelerator. Most of the technical issues have presently been satisfactorily addressed; the only serious one remaining is that of bonding for mechanical contact under heated conditions. This may be solved by a technique under development to use liquid indium layers, or may be circumvented by further development of a load design that does not use insulator discs in the path of the compression wave (leaving only solid-liquid interfaces).

6.2. Computational Study

Under the LDRD project, *ab initio* density-functional theory based molecular-dynamics simulations were performed for molten Sn over a range of temperatures and pressures. These simulations of the structure of a molten metal based on first-principles electronic-structure calculations push the current state of the art. The results for the liquid structure compare well with experimental static structure factors available at zero pressure. The calculations examined the variation of the structure with both temperature and pressure. No evidence was found of a liquid–liquid transition that had been speculated at the beginning of the program. The results can be used to gain information about the equation of state of the liquid. As an example, the specific heat was computed. The first-principles molecular-dynamics results provided a database for the determination of a new interatomic potential to describe molten Sn and the high-pressure solid-liquid interfaces. This potential was based on a novel form that combined aspects of potentials developed for metallic systems with aspects of potentials designed for tetrahedrally bonded semiconductors. These potentials were shown to reproduce well the static structure factors computed directly from the first-principle molecular dynamics.

Molecular-dynamics simulations with the interatomic potentials were used to address aspects of the kinetics of the solidification process. The velocity of the solid-liquid interface as a function of the

degree of under-cooling and/or over-pressurization was computed. These results allow a determination of the melt curve in the phase diagram. The computed liquidus was found to lie approximately 50 K above the experimental liquidus. It was found that the velocity of the interface scales linearly with the magnitude of the free energy difference between the solid and liquid phase, independent of whether that difference was due to under-cooling or over-pressurization. Aspects of homogeneous nucleation of the solid phase were investigated by calculating from the molecular-dynamics results the critical temperature for maximum over-heating of the solid phase. This information allows an estimation of both the maximum degree of under-cooling/over-pressurization of the liquid and the solid-liquid interfacial free energy at the temperatures and pressures of interest.

There are two major areas where there is a need for future work. The first is heterogeneous nucleation of the solid. It is known from studies of dynamic freezing in water [Dolan and Gupta, 2004] that solidification kinetics can depend on the nature of the container. This suggests that the solidification can nucleate at the container walls. The nature of the local structure of the melt in the vicinity of the wall and how that influences the nucleation of the solid is an important issue. Also, any characteristics of the container wall that would either inhibit or promote nucleation in the case of molten metals are of interest. The second major issue is the influence of alloy additions on the solidification process. Alloying will influence the solidification in many ways. It will alter the thermodynamic balance between the solid and liquid phases, as well as the solid-liquid interfacial free energies. Alloying is also expected to introduce additional rate dependence to the solidification process. In the limit of slow solidification, the composition is expected to equilibrate. This leads to segregation at the solid-liquid interface and to creation of solid phases near equilibrium compositions. In the rapid solidification limit, the local compositions will not be in equilibrium and this can have significant influence on the solidification. It would be of great interest to explore these issues in future work.

6.3. Future Directions

One original goal of the LDRD project was to incorporate information gleaned from the computational study into a new continuum model for liquid tin that includes realistic solidification kinetics and can faithfully reproduce the experimental results. Although this goal has not been accomplished, the existing computational results could be used to begin development of such a model. Specifically, the solid-liquid interface velocity (as a function of difference in free energy) could inform a model for the growth of the solid phase in the liquid, and the estimate for interfacial energy could inform a model for homogeneous nucleation. In addition, the result for maximum over-pressurization could be incorporated into a model for the strain-rate dependence of solidification. Further MD calculations could extend these results to higher pressures.

Ultimately, however, the ability to successfully and consistently model experiment using continuum models may depend on the ability to precisely control the level of impurities in the liquid tin sample. Further work, both computational and experimental, is needed to investigate the effects of impurities and alloying components on dynamic solidification. This area has particular importance to stockpile stewardship.

REFERENCES

Alchagirov, B.B. and Chochaeva, A.M., 2000, High Temperature **38**, 44.

Anderson, H.C., 1980, J. Chem. Phys. **72**, 2384.

Andrews, D.J., 1971, J. Comp. Phys. **7**, 310.

Asay, J.R. and Chhabildas, L.C., 1980, *High Pressure Science and Technology (Proceedings)*, Pergamon Press, 958.

Ashcroft, N.W. and Mermin, N.D., 1976, *Solid State Physics*, Holt, Rinehart and Winston.

Barker, L.M. and Hollenbach, R.E., 1970, J. Appl. Phys. **41**, 4208.

Bernard, S. and Maillet, J.B., 2002, Phys. Rev. B **66**, 012103.

Cheong, B.H. and Chang, K.J., 1991, Phys. Rev. B **44**, 4103.

Christensen, N.E., 1993a, Solid St. Comm. **85**, 151.

Christensen, N.E. and Methfessel, M., 1993b, Phys. Rev. B **48**, 5797.

Corkill, J.L., Garcia, A. and Cohen, M.L., 1991, Phys. Rev. B **43**, 9251.

Davis, J.-P., Deeney, C., Knudson, M.D., Lemke, R.W., Pointon, T.D. and Bliss, D.E., 2005, Phys. Plasmas **12**, 056310.

Davis, J.-P., 2005, Sandia National Laboratories Report SAND2005-2068.

Daw, M.S., Foiles, S.M. and Baskes, M.I., 1993, Materials Science Reports **9**, 251.

de Avillez, R.R., Lopes, M.F.S. and Silva, A.L.M., 1996, Mater. Sci. Eng. A **205**, 209.

Dolan, D.H. and Gupta, Y.M., 2004, J. Chem. Phys. **121**, 9050.

Eldred, M.S., Hart, W.E., van Bloemen Waanders, B.G., Giunta, A.A., Wojtkiewicz, S.F. Jr., and Alleva, M.P., Sandia National Laboratories Report SAND2003-3796.

Frenkel, D. and Smit, B. 1996, *Understanding Molecular Simulation: From Algorithms to Applications*, Academic Press.

Furnish, M.D., Davis, J.-P., Knudson, M.D., Bergstresser, T., Deeney, C. and Asay, J.R., 2001, Sandia National Laboratories Report SAND2001-3773.

Gamertsfelder, C., 1941, J. Chem. Phys. **9**, 450.

Glosli, J.N. and Ree, F.H., 1999, Phys. Rev. Lett. **82**, 4659.

Hall, C.A., Asay, J.R., Knudson, M.D., Stygar, W.A., Spielman, R.B., Pointon, T.D., Reisman, D.B., Toor, A. and Cauble, R.C., 2001, Rev. Sci. Instrum. **72**, 3587.

Hall, C.A., 2003, private communication.

Hamann, D., 1989, Phys Rev. B **40**, 2980.

Hansen, J.-P. and McDonald, I.R., 1986, *Theory of Simple Liquids, 2nd edition*, Academic Press.

Hayes, D.B., 1975, J. Appl. Phys. **46**, 3438.

Hayes, D.B., 2000, private communication.

Hayes, D.B., 2001, Sandia National Laboratories report SAND2001-1440.

Hemsing, W.F., 1979, Rev. Sci. Instrum. **50**, 73.

Horie, Y. and Duvall, G.E., 1968, *Behavior of Dense Media under High Dynamic Pressure* (IUTAM Symposium on High Dynamic Pressure), Gordon and Breach, 355.

Johnson, J.D., 1994, Los Alamos National Laboratory Report LA-UR-94-1451.

Katayama, Y., Mizutani, T., Utsumi, W., Shimomura, O., Yamakata, M. and Funakoshi, K., 2000, Nature **403**, 470.

Kaxiras, E., 2003, *Atomic and Electronic Structure of Solids*, Cambridge University Press.

Kerley, G.I., 1987, Int. J. Impact Engineering **5**, 441.

Kipp, M.E. and Lawrence, R.J., 1982, Sandia National Laboratories Report SAND81-0930.

Liu, L.-G. and Bassett, W.A., 1986, *Elements, Oxides, and Silicates: High Pressure Phases with Implications for the Earth's Interior*, Oxford University Press.

Luo, S.-N. and Ahrens, T.J., 2003a, Appl. Phys. Lett. **82**, 1836.

Lou, S.-N., Ahrens, T.J., Cagin, T., Strachan, T.A., Goddard III, W.A. and Swift, D.C., 2003b, Phys. Rev. B **68**, 134206.

Luo, S.-N., Strachan, A. and Swift, D.C., 2004, J. Chem. Phys. **120**, 11640.

Mabire, C. and Héreil, P.-L., 2000, J. Phys. IV **10**, Pr9/749.

Martin, R.M., 2004, *Electronic Structure: Basic Theory and Practical Methods*, Cambridge University Press.

Nasch, P.M. and Steinemann, S.G., 1995, Phys. Chem. Liq. **29**, 43.

North, D.M., Enderby, J.E. and Egelstaff, P.A., 1968, J. Phys. C (Proc. Phys. Soc.) Ser. 2, vol. 1, 1075.

Rappaz, M., Jacot, A., and Boettinger, W.J., 2003, Metall. Mater. Trans. A **34**, 467.

Shekar, N.V.C. and Rajan, K.G., 2001, Bull. Mater. Sci. **24**, 1.

So, W.W. and Lee, C.C., 2000, IEEE Trans. Components and Packaging Tech. **23**, 377.

Tefft, W.E., 1966, J. Research National Bureau of Standards **70A**, 277.

Tersoff, J., 1988, Phys. Rev. B **37**, 6991.

Thiele, J., 1963, J. Chem. Phys. **39**, 474.

Vahvaselkä, K.S., 1978, Physica Scripta **18**, 266.

Waseda, Y. and Suzuki, K., 1972, Phys. Stat. Sol. (b) **49**, 339.

Waseda Y., 1980, *The Structure of Non-Crystalline Materials: Liquids and Amorphous Solids*, McGraw-Hill.

Wertheim, M., 1963, Phys. Rev. Lett. **10**, 321.

Wright, A.F., 2003, private communication.

Zou, X.-W., Jin, Z.-Z. and Shang, Y.-J., 1987, Phys. Stat. Sol. (b) **139**, 365.

DISTRIBUTION

1	MS 0123	D. L. Chavez, 1011 (LDRD Program Office)
1	MS 1110	J. B. Aidun, 1435
1	MS 1110	M. G. Martin, 1435
1	MS 1110	A. P. Thompson, 1435
1	MS 1181	J. R. Asay, 1646
1	MS 1181	J.-P. Davis, 1646
1	MS 1181	D. H. Dolan, 1646
1	MS 1181	C. A. Hall, 1646
1	MS 1181	R. J. Hickman, 1646
1	MS 1181	M. D. Knudson, 1646
1	MS 1181	C. Deeney, 1640
1	MS 1192	J. L. Taylor, 1649 (Bechtel Nevada)
1	MS 1193	D. W. Droemer, 1649 (Bechtel Nevada)
1	MS 1411	H. E. Fang, 1814
1	MS 1411	S. M. Foiles, 1814
1	MS 1411	J. J. Hoyt, 1814
1	MS 1411	D. Olmsted, 1814
1	MS 1411	E. B. Webb, 1814
1	MS 0887	D. B. Dimos, 1800
1	MS 0885	R. J. Salzbrenner, 1820
2	MS 9018	Central Technical Files
2	MS 0899	Technical Library

1 Marina Bastea
MS L-286
Lawrence Livermore National Laboratory
7000 East Ave.
Livermore, CA 94550

1 Dennis Hayes
P. O. Box 591
Tijeras, NM 87059

1 Paulo Rigg
MS P952
Los Alamos National Laboratory
P. O. Box 1663
Los Alamos, NM 87545